DIPARTIMENTO DI INGEGNERIA CIVILE
Università degli Studi di Salerno

Dottorato di Ricerca in Rischio e Sostenibilitá nei Sistemi dell'Ingegneria Civile, Edile ed Ambientale

XXXVIII Ciclo

Tesi di dottorato in

Mechanics and Rapid Prototyping of Innovative Tensegrity Structures

Giovanni Germano

Tutor
Prof. Ada Amendola

Coordinatore
Prof. Fernando Fraternali

Co-tutor
Dr. Julia de Castro Motta

A.A. 2024-2025

Abstract

This doctoral dissertation investigates the mechanics, kinematics, and rapid prototyping of novel structural modules with tensegrity architecture, developed for advanced applications in structural engineering. These modules are conceived as adaptive systems capable of modifying their configuration and mechanical response through the control of a limited number of cables, whose rest lengths are appropriately adjusted to enable structural deployment and the formation of stable tensegrity configurations.

The mechanical properties of the modules, in terms of stiffness and load-carrying capacity, are regulated by modulating the pretension of the actuation cables once the deployment motion is constrained. The dissertation presents a systematic analysis of the kinematics and mechanics of the proposed structures, based on both analytical and numerical modeling, and investigates their behavior under different operational configurations. Particular emphasis is placed on the development and validation of rapid prototyping procedures, based on additive manufacturing technologies, aimed at the fabrication of physical models and the experimental assessment of structural performance.

The primary applications of the investigated structural systems concern adaptive structures for solar energy harvesting, with specific reference to devices that can be integrated into building envelopes or modular systems. However, the proposed design approach and the developed structural solutions are broadly applicable to a wider range of engineering contexts, including smart structural systems, passive and semi-active control devices for structural response, as well as applications in the field of seismic engineering.

Keywords

Origami systems, Tensegrity structures, Solar modules, Force-displacement response, Photovoltaics, Solar energy.

Publications

The research work carried out by the candidate during his Ph.D. career resulted in a collection of publications on the mechanics of advanced structural systems, including tensegrity–origami structures, metamaterials, and seismic isolators. Such publications comprise works directly related to the present thesis and additional research contributions by the candidate, as specified in what follows.

Bibliographic identifiers of the candidate

- Scopus ID: 58625857900
- ORCID ID: 0009-0009-7031-9491

Publications related to the present thesis work

Refereed Journal Articles

(P1) Fraternali, F, de Castro Motta, J., **Germano, G.**, Babilio, Amendola, A. (2024). *Mechanical response of tensegrity-origami solar modules.* Applications in Engineering Science, 17, 100174, 2024. DOI: 10.1016/j.apples.2023.100174

Other Publications in Refereed Journal Articles

Journal Articles

(O1) Adinolfi, V., **Germano, G.** (2025). *On the discrete assembly of additively manufactured pentamode lattices confined between stiffening plates.* Journal of the Brazilian Society of Mechanical Sciences and Engineering, 47(2), 70. DOI: 10.1007/s40430-024-05311-0

(O2) Fraternali, F., Babilio, E., Nazifi Charandabi, R., **Germano, G.**, Luciano, R., Spagnuolo, G. (2024) *Dynamic origami solar eyes with tensegrity architecture for energy harvesting Mashrabiyas.* Applications in Engineering Science 19,100190. DOI: 10.1016/j.apples.2024.100190

(O3) Qaderi, S., Adinolfi, V., **Germano, G.**, Benzoni, G., Luciano, R., Fraternali, F. (2023). *An experimental and mechanical study of a two-layer,*

bioinspired seismic isolator for multistory buildings. Buildings, 13(9), 2272. DOI: 10.3390/buildings13092272

(O4) **Germano G.**, Qaderi S., Adinolfi V., de Castro Motta, J., Benzoni, G., Amendola, A., Ruzzene, M., Fraternali, F. (2023). *Design and modeling of an in-house-built shake table setup for testing prototypes of innovative seismic isolators*, Ingegneria Sismica, 40(1), 59-72. ISSN: 03931420.

Refereed Conferences Proceedings

(C1) Adinolfi, V., Qaderi, S., **Germano, G.**, de Castro Motta, J., Benzoni, G., Amendola, A., Ruzzene, M., Fraternali, F. *Experimental testing of innovative, biomimetic seismic metaisolators*. 9th International Conference on Computational Methods in Structural Dynamics and Earthquake Engineering (COMPDYN 2023). DOI: 10.7712/120123.10584.20955

To my family

Acknowledgements

The author wishes to express sincere gratitude to the following individuals and colleagues for their valuable advice, collaboration, and support throughout the development of this work.

Supervisor and advisors

Ada Amendola (Supervisor), *Fernando Fraternali*, and *Giovanni Spagnuolo* (University of Salerno),
César Domínguez (Universidad Politécnica de Madrid).

Colleagues

Julia De Castro Motta, Valentina Adinolfi, Giuseppina Di Chiara, Hazar Etteyeb, Angela Lato, Rana Nazifi Charandabi, Ilaria Passegiato (University of Salerno).

A special expression of gratitude is reserved for my family and friends, whose constant encouragement and support provided strength and motivation throughout the past three years.

Thank you all.

Contents

List of Figures

1

Introduction

The development of adaptive structural systems capable of modifying their configuration and mechanical response in a controlled manner represents a central theme in contemporary structural engineering. Such systems offer significant potential for applications where deployability, reconfigurability, and tunable stiffness are required to meet changing functional or environmental demands. In this context, the building envelope constitutes a relevant but non-exclusive domain of application, as adaptive structures can also be employed in a wide range of engineering fields, including seismic protection, lightweight deployable systems, and smart structural components.

Among the approaches proposed to achieve structural adaptability, origami-inspired systems have attracted increasing interest due to their inherent deployability, geometric versatility, and efficient use of material. Origami-based structures enable the realization of thin-walled, foldable systems characterized by multistability, high packing efficiency, and programmable kinematic behavior (Miura, 1985; Seffen, 2012; Schenk and Guest, 2013; Zhai et al., 2018; Pratapa et al., 2018; Li and Pellegrino, 2020; Lu et al., 2023a; Lu et al., 2023b). These characteristics have motivated applications spanning robotics, biomedical devices, aerospace engineering, and architecture (Fonseca et al., 2022; Salazar et al., 2017; Liu et al., 2023). In architectural engineering, origami principles have been employed to design adaptive façade systems and shading devices, such as the kinetic façade of the Al Bahar Towers in Abu Dhabi, where folding triangulated elements provide dynamic environmental control (Armstrong et al., 2013; Karanouh and Kerber, 2015). Related developments include kaleidocycle-based adaptive façades (Elghazi et al., 2014; Wagdy et al., 2015), shape-memory–actuated origami systems (Pesenti et al., 2015), and self-deploying structures fabricated from programmable materials (Chen et al., 2019).

More recently, origami concepts have been reinterpreted within the framework of tensegrity theory, leading to lightweight structural systems composed of discontinuous compression elements stabilized by networks of prestressed cables. Tensegrity-based systems are particularly attractive from a structural engineering perspective, as their global stiffness, stability, and load-bearing capacity can be modulated through the control of cable pretension, rather than through rigid-body mechanisms. Hybrid tensegrity–origami structures activated by cable-driven control strategies have demonstrated the ability to achieve controlled deployment and reconfiguration while maintaining structural efficiency and reduced actuation demands (Fraternali et al., 2015a; Mi-

randa et al., 2020).

Within this broader framework, energy-harvesting systems represent one of several possible application domains for adaptive tensegrity–origami structures. The integration of photovoltaic or thermal components into reconfigurable structural elements has motivated the development of dynamic shading devices and sun-tracking systems (Gao et al., 2018; Vassiliades et al., 2022). However, such energy-related applications should be regarded as a specific case study rather than the primary objective, as the underlying structural concepts are applicable to a wider range of engineering problems, including vibration control, deployable protective systems, and adaptive seismic-resilient structures.

In this context, the present thesis introduces a new class of adaptive tensegrity–origami modules, conceived as mechanically efficient, deployable structural systems with controllable kinematics and tunable mechanical response. The proposed modules, referred to as "tensori" units, are designed to tessellate planar or curved surfaces and to operate as modular components in a variety of engineering applications. Each unit consists of interconnected rigid elements and prestressed cables arranged to form a tensegrity-based origami structure capable of undergoing controlled deployment and reconfiguration through the regulation of a limited number of control cables.

The proposed system exhibits two independent folding motions: a primary folding mechanism governing the deployment and compaction of the structural unit, and a secondary folding mechanism enabling additional relative rotations between selected rigid elements. These motions allow the system to transition between multiple stable or semi-stable configurations and to adapt its mechanical properties, such as stiffness and load transfer characteristics, to different operational requirements. The integration of energy-harvesting components within the rigid elements is investigated as one representative application, alongside other potential uses in adaptive structural engineering and seismic control.

The thesis develops the proposed concept through a progressive investigation. Chapter 2 addresses the geometric design principles and kinematic characterization of the tensegrity–origami modules, with particular emphasis on quadrilateral configurations and deployability. Chapter 3 investigates the mechanical behavior of the system, including stiffness modulation through cable pretension, stability of deployed configurations, and dynamic response under external loading. Chapter 4 presents the rapid prototyping and experimental

validation of a representative module fabricated using additive manufacturing techniques, detailing component design, assembly procedures, admissible motions, and actuation strategies (Fraternali et al., 2024b). Building on the single-module analysis, Chapter 5 explores multi-module assemblies and tessellation strategies, while Chapter 6 presents the mechanical design, kinematics, and manufacturing of a smart PV window prototype (SMARTWIN), equipped with a dedicated actuation system. Finally, Chapter 7 summarizes the main outcomes of the work and outlines future research directions for adaptive tensegrity–origami systems in structural engineering.

2

Kinematics of Tensegrity-Origami Modules

The present chapter, together with the subsequent Chapters 3 and 4, collects and further develops results originally presented in the following bibliographic paper, coauthored by the PhD candidate and cited in the bibliography as Fraternali et al., 2024b:

Fraternali, F., de Castro Motta, J., **Germano, G.**, Babilio, E., Amendola, A. (2024). *Mechanical response of tensegrity–origami solar modules. Applications in Engineering Science*, 17, 100174. ISSN: 2666–4968. DOI: 10.1016/j.apples.2023.100174.

2.1 Design principles of tensegrity-origami modules

The solar modules investigated in this thesis are characterized, in the plane parallel to the building façade, by a polygonal planform. In correspondence to the unfolded (or 'closed') configuration, such a planform is referred to as the 'base polygon', and p denotes its number of sides. As illustrated in Fig. 2.1, the module is assembled from p foldable 'macro-triangles', each defined by the segments that connect a vertex of the base polygon to its center. Each macro-triangle is, in turn, partitioned into two elementary 'micro-triangles' accommodating PV or T panels, which rotate out of the initial plane during the opening/closing of the screen (hereafter, 'sunscreen panels'). The cables associated with such a ('primary') folding mechanism link the vertices of the folded macro-triangles to the center of the unit (opening cables) and to the corners of the base polygon (closing cables). These members are connected to a perimeter 'bus cable' running along the base polygon, enabling the simultaneous actuation of the opening/closing mechanisms across the different micro-triangles (see Sect. 2.2 for additional details). Examples of solar façades obtained by tessellating origami modules with distinct geometries are reported in Fig. 2.2.

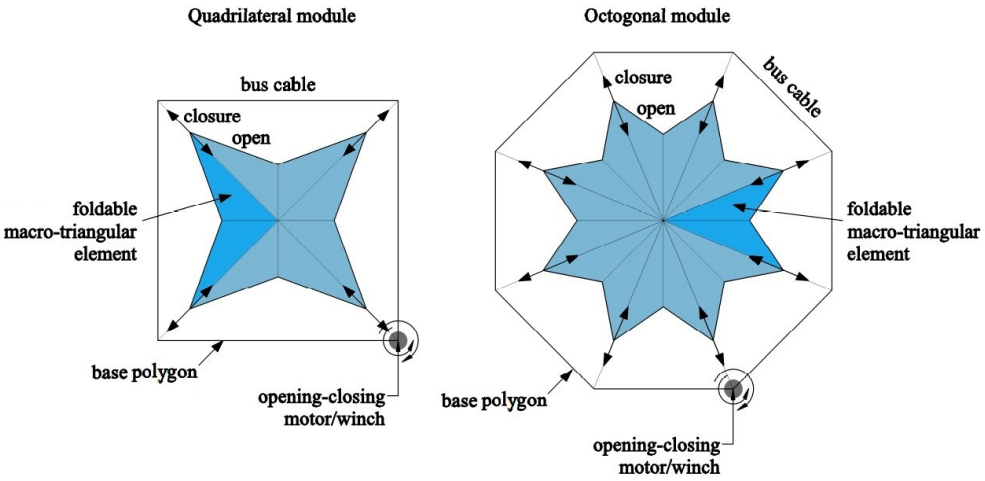

Figure 2.1: Frontal views of quadrilateral and octagonal versions of the solar eye module, with illustration of the primary folding motion (reproduced from Fraternali et al., 2024b under the license CC BY-NC-ND 4.0).

The folding/deformation of the module is achieved by varying the cables' rest lengths without inducing cable stretch, differently from the system considered in (Miranda et al., 2020), where folding is driven by elastic deformation of the perimeter cables. The required adjustment of rest length may be provided either by low-power electric winches or motors, or manually by crank winches (Fig. 2.1). When the activation winches/motors are locked, the rest lengths of the 'primary motion activation cables' remain fixed and the configuration is stable, since deviations from such an equilibrium are resisted by the elastic stiffness and the prestress-induced (or 'geometric') stiffness of the cables (Fraternali et al., 2015a). Conversely, when the actuation devices are unlocked and rest-length variations are allowed, the unit undergoes an out-of-plane rigid-body folding (or 'opening') motion (cf. Fig. 2.1).

Sun-tracking is enabled by introducing a secondary folding mode affecting the micro-triangle plates, whereby these plates rotate about the 'diagonal' edges (or 'legs') that connect the perimeter vertices to the center of the module (see Fig. 2.3). The evolution of the dihedral angle θ between the supporting frame of the micro-triangle ('base plane') and the rotated plate ('folded plane') is controlled by a two-bar scissor-like tensegrity linkage connecting the two planes (the term 'scissor' refers to the near-closed arrangement, see Fig. 2.3).

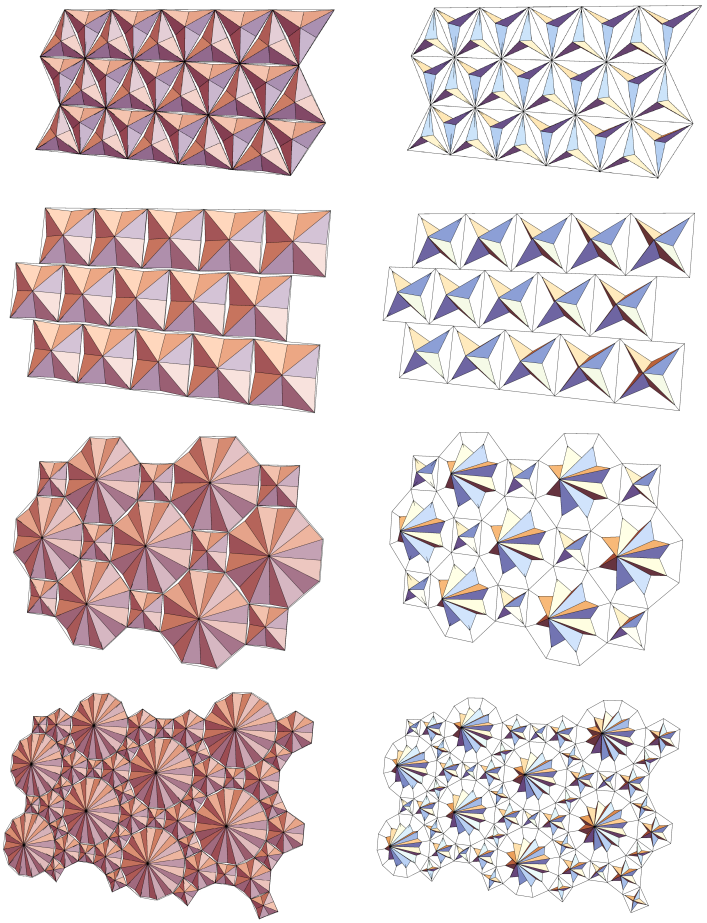

Figure 2.2: Partially closed (left) and partially open (right) configurations of origami solar facades with different textures.
The textures of the two top panels are composed of modules with identical shapes. Those of the two bottom panels are instead formed by composite assemblies of modules with different polygonal shapes (reproduced from Fraternali et al., 2024b under the license CC BY-NC-ND 4.0).

Each bar terminates at one end in a ball joint attached to the folded plane, located at a distance c from the diagonal edge (Fig. 2.3); the opposite end is connected to a guiding cable lying in the base plane. One bar is coupled, at its lower extremity, to an opening cable (red in Fig. 2.3), while the other is

coupled to a closing cable (brown in Fig. 2.3). Both are connected to a looped bus cable (green in Fig. 2.3), so that opening and closing can be commanded through a single controller.

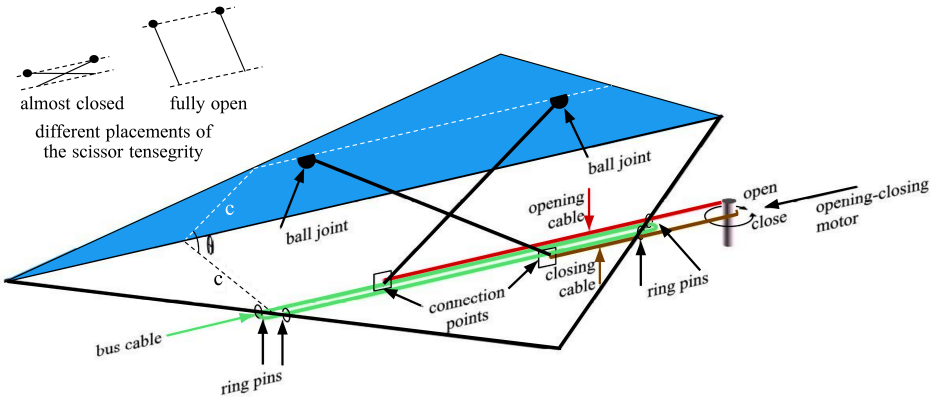

Figure 2.3: Illustration of the secondary folding motion of a micro-triangle (reproduced from Fraternali et al., 2024b under the license CC BY-NC-ND 4.0).

In what follows, the cables shown in Fig. 2.3 are termed 'secondary motion activation cables'. The two scissor bars connect to distinct edges of the folded micro-triangle, namely the edges opposite the diagonal one. During folding, their motion is symmetric with respect to the central axis of the linkage: in the unfolded (or closed) configuration they lie parallel to the supporting frame, whereas in the fully folded (or open) configuration they approach an orientation orthogonal to it (see Fig. 2.3). Control of the secondary motion is again obtained by changing the rest lengths of the scissor-base cables via electric winches/motors or crank winches, similarly to the primary motion. When the corresponding actuator is locked and an appropriate pretension is assigned to the base cables, the secondary motion is stabilized by constraining their rest lengths, so that perturbations are counteracted by both material stiffness and geometric stiffness of the cables (Fraternali et al., 2015a). Under external actions (e.g., wind loads), the scissor bars deflect the secondary cables of the stabilized system, leading to a tensegrity equilibrium state (see Fig. 2.4 and Sect. 3.1.2).

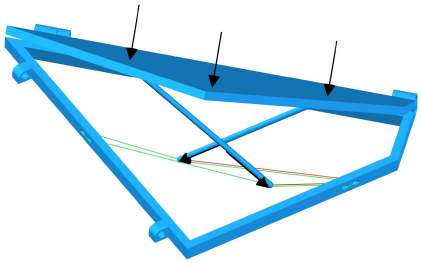

Figure 2.4: Deformation of the base cable of the scissor tensegrity under the action of external forces (reproduced from Fraternali et al., 2024b under the license CC BY-NC-ND 4.0).

2.2 The special case of a quadrilateral module

We now consider the quadrilateral solar-eye module, comprising four macro-triangles and eight micro-triangles, the latter incorporating PV and/or T panels (black elements in Fig. 2.5). The solutions and construction strategies discussed for this geometry readily extend to modules based on other polygonal base shapes.

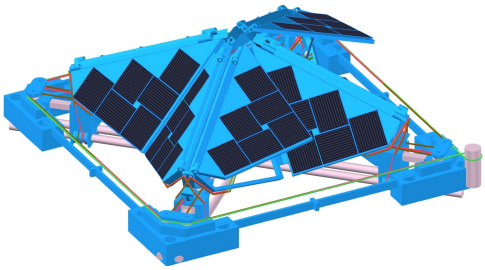

Figure 2.5: Illustrative isometric view of the quadrilateral module (reproduced from Fraternali et al., 2024b under the license CC BY-NC-ND 4.0).

In the quadrilateral case, the opening and closing cables driving the primary folding motion (i.e., the primary activation cables) are routed through guiding pulleys located at the four corners of the base perimeter, at the module center, and at the sliding blocks positioned along the diagonal edges (Fig. 2.6). Each slider travels along a diagonal track and is connected to one opening and one closing cable; such a pair actuates the primary motion of two micro-triangles arranged on opposite sides of the corresponding diagonal segment.

Overall, four sets of opening/closing cables are employed for the primary motion. All activation cables are merged into a single bus cable running along the base perimeter, which is connected to a winch/motor so that primary folding can be triggered simultaneously for all macro-triangles of the unit. The actuation of the secondary folding motion follows the scheme described in the previous section.

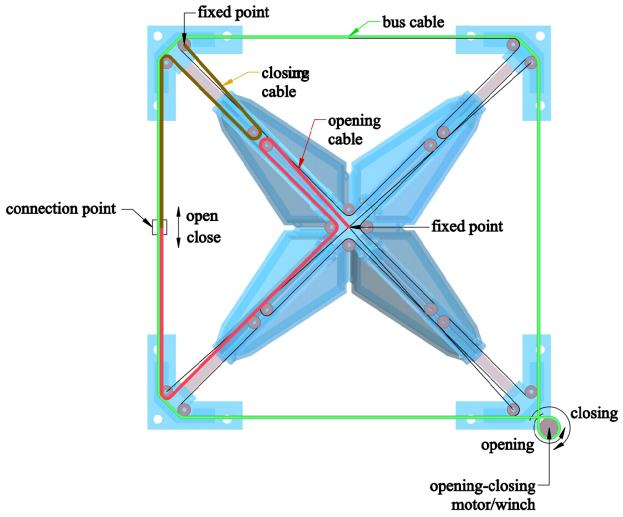

Figure 2.6: Opening-closing mechanism of the primary folding motion of a quadrilateral module obtained by changing the rest length of the activation cables (reproduced from Fraternali et al., 2024b under the license CC BY-NC-ND 4.0).

A demonstrator of the quadrilateral module was fabricated and assembled at the Rapid Prototyping Laboratory (RPL) of the University of Salerno using standard 3D printers, metallic components, DC motors, and motor drivers (Fig. 2.7). The prototype fits within a square of edge 290.22 mm and comprises eight right micro-triangles with hypotenuse 183 mm; the maximum elevation above the base supporting frame is 89.2 mm.

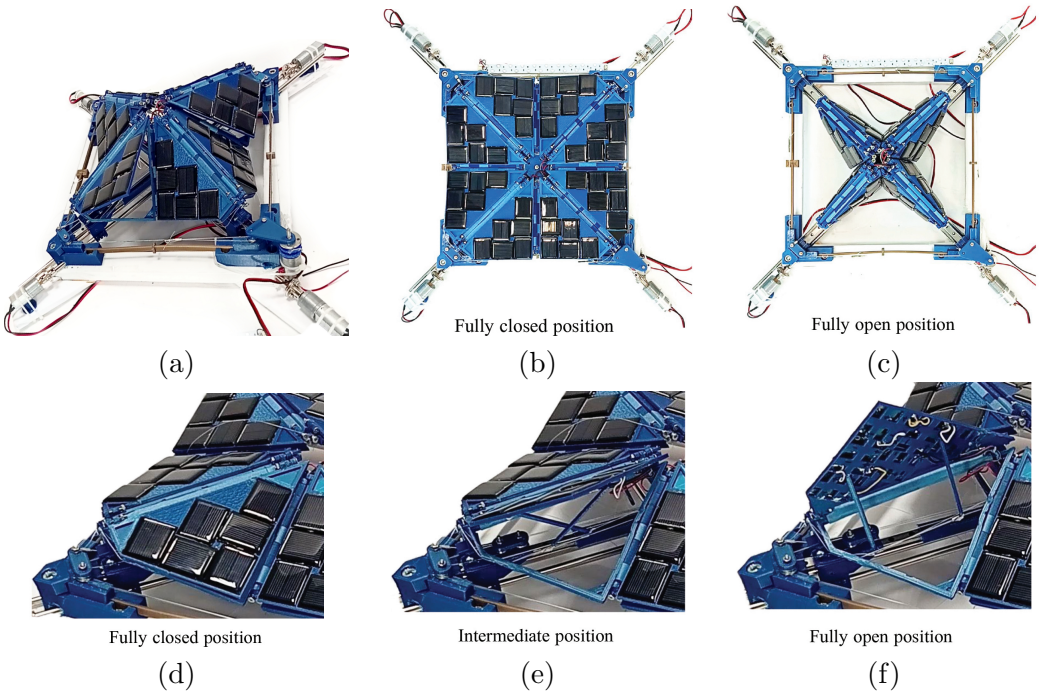

Figure 2.7: (a) 3D view of the fabricated mock-up of a quadrilateral module. (b-f) Frames extracted from videos of the opening and closing mechanisms of the primary (b-c) and the secondary (d-f) folding motions (reproduced from Fraternali et al., 2024b under the license CC BY-NC-ND 4.0).

2.3 Kinematics of the primary folding motion

Let $\mathcal{F}$ denote a generic macro-triangle within the unit cell of a solar module of polygonal planform. We assume $\mathcal{F}$ to be isosceles, with apex angle $0 < \alpha < \pi$ (Fig.2.8). In the analogous systems examined in (Miranda et al., 2020), such an angle is fixed and equal to $2\pi/3$. The unfolded (flat) placement is adopted as reference, and a Cartesian frame is introduced with origin at node 0 in Fig.2.8 and basis $\{\mathbf{e}_1, \mathbf{e}_2, \mathbf{e}_3\}$, where $\mathbf{e}_1$ is aligned with a diagonal edge (or leg) of $\mathcal{F}$, $\mathbf{e}_2$ lies in the reference plane and is orthogonal to $\mathbf{e}_1$, and $\mathbf{e}_3$ is normal to such a plane (Fig.2.8).

We analyze the primary folding deformation (quasi-static motion) of $\mathcal{T}$ under the following *displacement constraints*: node 0 moves along the positive $\mathbf{e}_3$ axis; node 1 translates along the 0–1 segment of the reference configuration;

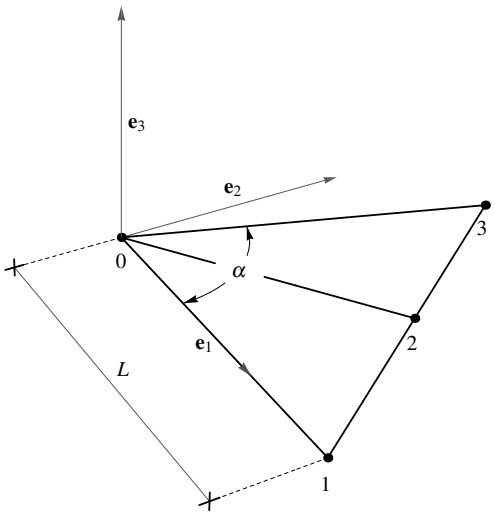

Figure 2.8: Reference configuration of the generic macro triangle $\mathcal{T}$. (reproduced from Fraternali et al., 2024b under the license CC BY-NC-ND 4.0).

node 2 is constrained to the plane spanned by $\mathbf{e}_3$ and the bisector of the angle α in the reference configuration, with a negative displacement component along $\mathbf{e}_3$; and the displacement of node 3 is obtained by rotating that of node 1 by an angle α about $\mathbf{e}_3$. In addition, a rigid-origami motion is enforced by complementing the above conditions with the *rigidity constraints*

$$L_{0i} = \ell_{0i}\,, \quad i = 1, 2, 3 \tag{2.1}$$

$$L_{2j} = \ell_{2j}\,, \quad j = 1 \text{ or } j = 3 \tag{2.2}$$

where L_{ij} and ℓ_{ij} denote the Euclidean distances between nodes i and j in the reference and folded configurations, respectively. Such distances are computed through

$$L_{ij} = \sqrt{(\mathbf{X}_i - \mathbf{X}_j) \cdot (\mathbf{X}_i - \mathbf{X}_j)}\,, \tag{2.3}$$

$$\ell_{ij} = \sqrt{(\mathbf{x}_i - \mathbf{x}_j) \cdot (\mathbf{x}_i - \mathbf{x}_j)}\,. \tag{2.4}$$

Here, $\mathbf{X}_i$ and $\mathbf{x}_i$ are the position vectors of node $i \in \{0, 1, 2, 3\}$ in the reference and folded placements. From Fig.2.8 one obtains $L_{01} = L_{03} = L$, $L_{21} = L_{23} = L\sin(\alpha/2)$, and $L_{02} = L\cos(\alpha/2)$.

Let $\mathbf{R}_\alpha = \mathbf{R}(\alpha)$ denote the rotation tensor

$$\begin{aligned}\mathbf{R}(\alpha) := &\cos\alpha\,(\mathbf{e}_1\otimes\mathbf{e}_1 + \mathbf{e}_2\otimes\mathbf{e}_2)\\ &+\sin\alpha\,(\mathbf{e}_2\otimes\mathbf{e}_1 - \mathbf{e}_1\otimes\mathbf{e}_2) + \mathbf{e}_3\otimes\mathbf{e}_3,\end{aligned} \tag{2.5}$$

which applies a counterclockwise rotation of angle α to vectors in the $\mathbf{e}_1$–$\mathbf{e}_2$ plane. Accordingly (Fig.2.8),

$$\mathbf{X}_0 = \mathbf{0}\,, \tag{2.6}$$

$$\mathbf{X}_1 = L\mathbf{e}_1\,, \tag{2.7}$$

$$\mathbf{X}_2 = L\cos\frac{\alpha}{2}\left(\cos\frac{\alpha}{2}\mathbf{e}_1 + \sin\frac{\alpha}{2}\mathbf{e}_2\right)\,, \tag{2.8}$$

$$\mathbf{X}_3 = \mathbf{R}_\alpha\mathbf{X}_1\,, \tag{2.9}$$

and the displacement constraints lead to

$$\mathbf{x}_0 = \mathbf{X}_0 + a_0 L\mathbf{e}_3\,, \tag{2.10}$$

$$\mathbf{x}_1 = \mathbf{X}_1 - a_1 L\mathbf{e}_1\,, \tag{2.11}$$

$$\mathbf{x}_2 = \mathbf{X}_2 - a_2 L\left(\cos\frac{\alpha}{2}\mathbf{e}_1 + \sin\frac{\alpha}{2}\mathbf{e}_2\right) - a_3 L\mathbf{e}_3\,, \tag{2.12}$$

$$\mathbf{x}_3 = \mathbf{R}_\alpha\mathbf{x}_1\,, \tag{2.13}$$

with the admissibility conditions

$$a_0 \geq 0, \quad 0 \leq a_1 \leq 1, \quad 0 \leq a_2 \leq \cos\frac{\alpha}{2}, \quad a_3 \geq 0. \tag{2.14}$$

The dimensionless parameters a_i ($i = \{0,\ldots,3\}$) in Eqns. (2.10)–(2.14) are determined by enforcing the rigidity constraints. For later reference, we introduce

$$L_{13}(1-\varepsilon) = \ell_{13}\,, \tag{2.15}$$

where $\varepsilon \geq 0$ represents either the variation of rest length of the closure cable 1–3 (deployment) or the opposite of the engineering strain associated with its stretching (stabilization). Squaring Eqns. (2.1)–(2.2) and rearranging terms yields a system of nonlinear algebraic relations that can be cast as

$$a_0^2 + a_1\,(a_1 - 2) = 0\,, \tag{2.16}$$

$$(a_0 + a_3)^2 + a_2\left(a_2 - 2\cos\frac{\alpha}{2}\right) = 0\,, \tag{2.17}$$

$$a_1^2 + a_2^2 + a_3^2 + a_1\left(\cos\alpha - 2a_2\cos\frac{\alpha}{2} - 1\right) = 0. \tag{2.18}$$

An additional relation follows from Eqn. (2.15), namely

$$\varepsilon^2 + 2\,(a_1 - \varepsilon) \;-\; a_1^2 = 0. \tag{2.19}$$

The system (2.16)–(2.19) admits eight solution branches for the unknowns a_i, but only one is compatible with (2.14), i.e.,

$$a_0 = \sqrt{\varepsilon\,(2-\varepsilon)}\,, \tag{2.20}$$

$$a_1 = \varepsilon\,, \tag{2.21}$$

$$a_2 = \frac{\varepsilon}{2}\,\frac{\sin\alpha + 2\cos\frac{\alpha}{2}}{1-(1-\varepsilon)\sin\frac{\alpha}{2}}\,, \tag{2.22}$$

$$a_3 = \sqrt{\varepsilon\,(2-\varepsilon)}\;\sin\frac{\alpha}{2}\;\frac{1-\varepsilon-\sin\frac{\alpha}{2}}{1-(1-\varepsilon)\sin\frac{\alpha}{2}}\,. \tag{2.23}$$

The parameter ε attains its upper bound, denoted $\varepsilon_{\max}$, in the fully folded configuration of $\mathcal{T}$. Define $a_{2,\max}$ as the value of a_2 obtained by setting $\varepsilon = \varepsilon_{\max}$ in Eqn. (2.22). Enforcing the third condition in (2.14) yields

$$a_{2,\max} = \cos\frac{\alpha}{2}\,, \tag{2.24}$$

and Eqn. (2.22) then implies

$$\varepsilon_{\max} = 1 - \sin\frac{\alpha}{2}\,. \tag{2.25}$$

Figure 2.9 reports the dependence of $\varepsilon_{\max}$ on α as prescribed by Eqn. (2.25). Figure 2.10 collects the solution curves (2.20)–(2.23), including representative plots of $a_2(\varepsilon)$ and $a_3(\varepsilon)$ for selected values of α. It is also instructive to evaluate the asymptotic limits of a_1, a_2, and $\varepsilon_{\max}$ as $\alpha \to 0$ and as $\alpha \to \pi$. By combining Eqns. (2.20)–(2.23) with Eqn. (2.25), one finds that, for $\alpha \to 0$, $a_2 \to a_1$, $a_3 \to 0$, and $\varepsilon_{\max} \to 1$; whereas, for $\alpha \to \pi$, $a_2 \to 0$, $a_3 \to -a_0$, and $\varepsilon_{\max} \to 0$.

We close this section by noting that the primary folding deformation of a micro-triangle in $\mathcal{T}$ can be expressed in compact form. Consider, for instance, the deformation of $\overset{\triangle}{012}$ and introduce the 3×3 matrices

$$\begin{aligned} \hat{\mathbf{X}} \;&= \Big\{ \hat{\mathbf{X}}_1 - \hat{\mathbf{X}}_0 \;\Big|\; \hat{\mathbf{X}}_2 - \hat{\mathbf{X}}_0 \;\Big|\; \hat{\mathbf{X}}_4 - \hat{\mathbf{X}}_0 \Big\}, \\ \hat{\mathbf{x}} \;&= \big\{ \hat{\mathbf{x}}_1 - \hat{\mathbf{x}}_0 \;\big|\; \hat{\mathbf{x}}_2 - \hat{\mathbf{x}}_0 \;\big|\; \hat{\mathbf{x}}_4 - \hat{\mathbf{x}}_0 \big\} \end{aligned} \tag{2.26}$$

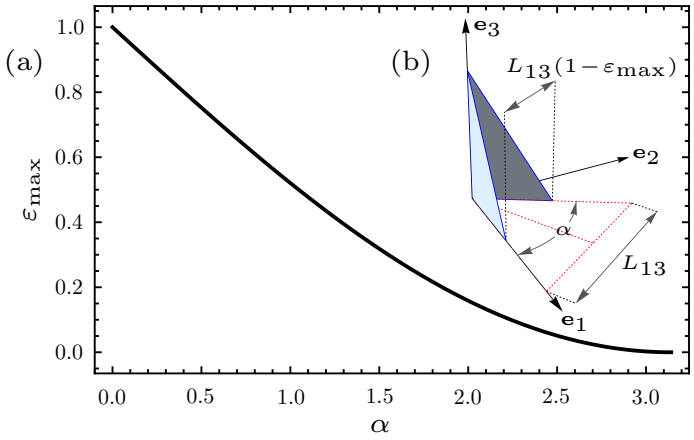

Figure 2.9: (a) Plot of $\varepsilon_{\max}$ vs. α. (b) Illustration of the fully folded configuration (reproduced from Fraternali et al., 2024b under the license CC BY-NC-ND 4.0).

where $\hat{\mathbf{X}}_i$ and $\hat{\mathbf{x}}_i$ collect the Cartesian components of $\mathbf{X}_i$ and $\mathbf{x}_i$ $(i = 0, \ldots, 4)$, respectively, and

$$\mathbf{X}_4 = \mathbf{X}_0 + \frac{(\mathbf{X}_1 - \mathbf{X}_0) \times (\mathbf{X}_2 - \mathbf{X}_0)}{S}\,, \tag{2.27}$$

$$\mathbf{x}_4 = \mathbf{x}_0 + \frac{(\mathbf{x}_1 - \mathbf{x}_0) \times (\mathbf{x}_2 - \mathbf{x}_0)}{s}\,, \tag{2.28}$$

with

$$S = ||(\mathbf{X}_1 - \mathbf{X}_0) \times (\mathbf{X}_2 - \mathbf{X}_0)|| \tag{2.29}$$

and

$$s = ||(\mathbf{x}_1 - \mathbf{x}_0) \times (\mathbf{x}_2 - \mathbf{x}_0)||\,. \tag{2.30}$$

Here, $\times$ denotes the vector cross product. It then follows that

$$\hat{\mathbf{x}}_i = \hat{\mathbf{x}}_0 + \hat{\mathbf{R}}'(\hat{\mathbf{X}}_i - \hat{\mathbf{X}}_0) \qquad (i = 1, 2), \tag{2.31}$$

where $\hat{\mathbf{R}}'$ is the rotation matrix defined by (Sumner and Popović, 2004)

$$\hat{\mathbf{R}}' = \hat{\mathbf{x}}\hat{\mathbf{X}}^{-1}. \tag{2.32}$$

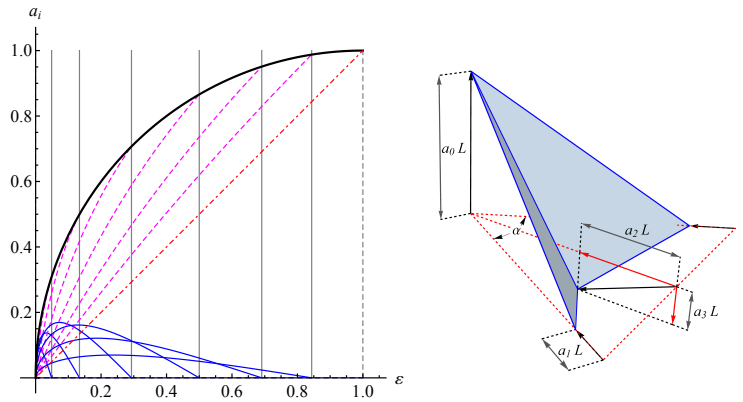

(a) (b)

Figure 2.10: (a) Plots of the displacement parameters a_i vs. ε, as given by Eqns. (2.20)-(2.23). The solid black curve plots a_0 vs. ε; the dash-dotted red line gives a_1 as a function of ε; the dashed magenta curves and the solid blue curves respectively plot the a_2 vs. ε and the a_3 vs. ε laws, which correspond to the following values of α, from left to right: $4\pi/5$, $2\pi/3$, $\pi/2$, $\pi/3$, $\pi/5$, $\pi/10$. (b) Illustration of the geometric meaning of the a_i parameters (reproduced from Fraternali et al., 2024b under the license CC BY-NC-ND 4.0).

An analogous construction applies to the second micro-triangle $\overset{\triangle}{023}$ of $\mathcal{T}$. Two representative folded states are shown in Fig. 2.11. Introducing the second-order rotation tensor $\mathbf{R}'$ (represented by $\hat{\mathbf{R}}'$ in the frame $\{\mathbf{e}_1, \mathbf{e}_2, \mathbf{e}_3\}$), Eqn. (2.31) can be rewritten in absolute vector form as

$$\mathbf{x}_i = \mathbf{x}_0 + \mathbf{R}'(\mathbf{X}_i - \mathbf{X}_0) \qquad (i = 1, 2). \tag{2.33}$$

2.4 Kinematics of the secondary folding motion

The secondary folding of a generic micro-triangle (for instance, $\overset{\triangle}{023}$ in Fig. 2.12) maps the vectors $\mathbf{x}_i$ into updated vectors $\mathbf{y}_i$ $(i = 0, 2, 3)$ according to

$$\mathbf{y_i} = \mathbf{R}''\mathbf{x_i} \tag{2.34}$$

where $\mathbf{R}''$ is the rotation tensor associated with an angle θ about the axis $\mathbf{x}_3 - \mathbf{x}_0$ (Fig. 2.12). For any θ, $\mathbf{y}_0$ and $\mathbf{y}_3$ coincide with $\mathbf{x}_0$ and $\mathbf{x}_3$, respectively, while $\mathbf{y}_2 \neq \mathbf{x}_2$ whenever $\theta \neq 0$. We next characterize the motion of the

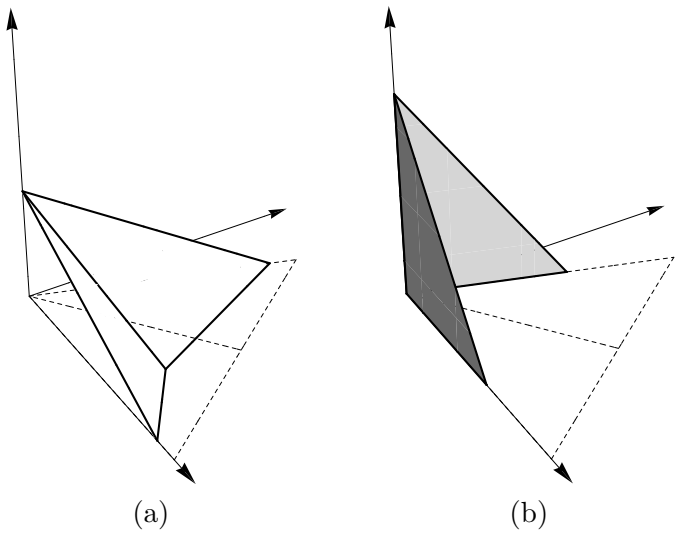

Figure 2.11: (a) Partially folded (open) configuration of $\mathcal{T}$. (b) Fully folded configuration (reproduced from Fraternali et al., 2024b under the license CC BY-NC-ND 4.0).

scissor linkage that connects the supporting frame through $\mathbf{x}_0$, $\mathbf{x}_2$, $\mathbf{x}_3$ to the folded plate with vertices $\mathbf{y}_0$, $\mathbf{y}_2$, $\mathbf{y}_3$. For simplicity, the two bars of the scissor structure are idealized as line segments of negligible thickness. During secondary folding, the two members evolve symmetrically with respect to the normal to the base cable through its midpoint; consequently, it suffices to describe the kinematics of the bar depicted in Fig. 2.12(b). Let a be the bar length, b the offset between the top ball joint and the boundary of the folded micro-triangle measured along $\mathbf{x}_3$–$\mathbf{x}_0$, and c the perpendicular distance from the segment $\mathbf{x}_3$–$\mathbf{x}_0$ to the base cable. The base-cable length is

$$L_c = L - \frac{2c}{\tan(\alpha/2)}. \tag{2.35}$$

To ensure a horizontal placement of the bar in the fully closed configuration, a must satisfy

$$a \leq L_c - b. \tag{2.36}$$

Here we assume $b \ll L_c$. The instantaneous configuration of the bar is described by the abscissa p of its lower end measured along the base cable (the 'base coordinate' in Fig. 2.12(b)).

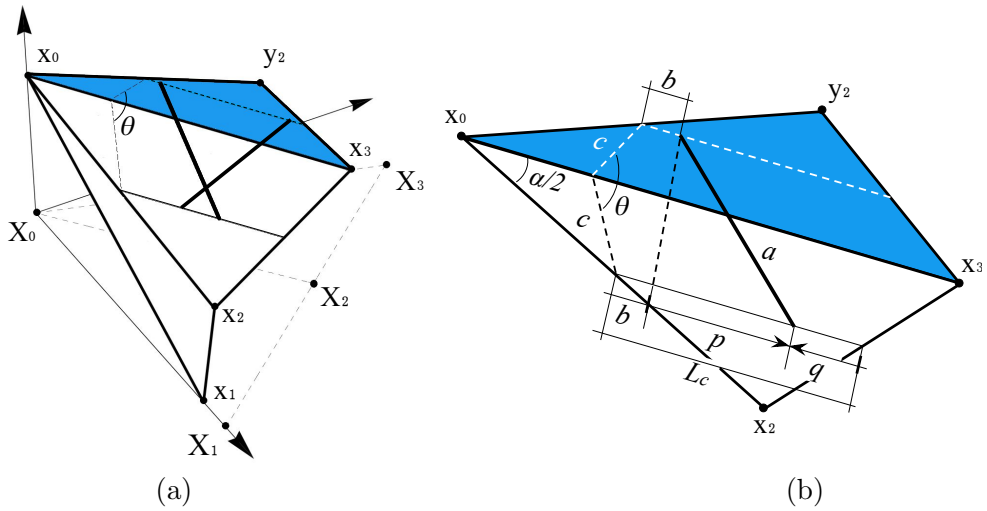

Figure 2.12: Geometry of the secondary folding motion of the micro-triangle $\overset{\triangle}{023}$. (a) Global view. (b) Close up of the folded plate (reproduced from Fraternali et al., 2024b under the license CC BY-NC-ND 4.0).

Elementary geometry gives

$$a^2 - p^2 = 2c^2 - 2c^2(\cos\theta)\,, \tag{2.37}$$

which yields p as a function of θ:

$$p(\theta) = \sqrt{a^2 + 2c^2(\cos\theta - 1)}, \qquad \text{with} \quad -b \le p \le a. \tag{2.38}$$

In the fully closed placement, $\theta = 0$ and hence $p = a$. In the fully open placement, $p = 0$ (see Fig. 2.3 and Fig. S9), and the maximum folding angle follows as

$$\theta_{max} = \arccos\left(1 - \frac{a^2}{2c^2}\right). \tag{2.39}$$

Accordingly, a target θ_{max} may be achieved by appropriate choices of a and c, for instance via

$$c = \frac{a}{\sqrt{2(1 - \cos\theta_{max})}}\,, \tag{2.40}$$

and inversion of Eqn. (2.38) gives

$$\theta(p) = \arccos\left(\frac{p^2 - a^2 + 2c^2}{2c^2}\right) \tag{2.41}$$

Figure 2.13 reports θ as a function of p for $a = 1$ and several values of c.

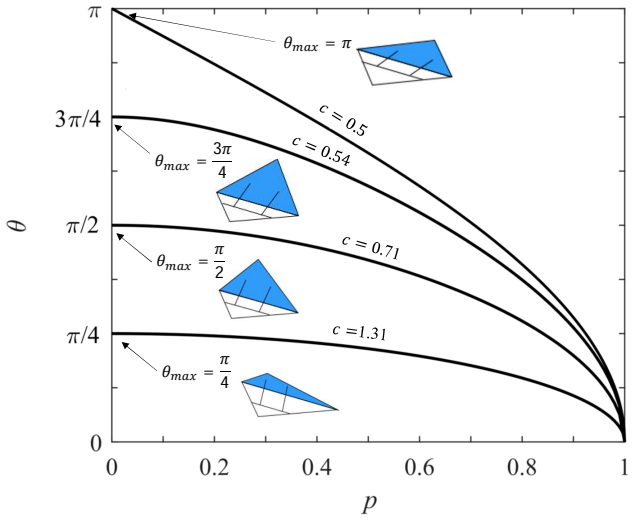

Figure 2.13: Opening angle θ as a function of the base coordinate p, for $a = 1$ and different values of c. The insets show the configuration of the micro-triangle in the fully open placement ($\theta = \theta_{max}$) (reproduced from Fraternali et al., 2024b under the license CC BY-NC-ND 4.0).

We finally introduce the second base coordinate q shown in Fig. 2.12, defined by

$$q = L_c - b - p, \qquad \text{with} \quad 0 \leq q \leq L_c. \tag{2.42}$$

Combining Eqns. 2.38 and 2.42 provides q as a function of θ:

$$q(\theta) = L_c - b - \sqrt{a^2 + c^2(\cos\theta - 1)}. \tag{2.43}$$

3

Mechanics of Tensegrity-Origami Modules

3.1 Stabilization of folding motions

The present Chapter addresses the response of the solar-eye module when stabilization is enforced by keeping cable rest lengths constant (i.e., with the activation winches/motors locked). The stabilization of the primary and secondary folding motions is examined separately in Sects. 3.1.1 and 3.1.2. In both cases, the force–displacement behavior of a selected portion $\mathcal{P}$ of the module is evaluated by prescribing a time-dependent history of a chosen displacement component while maintaining the actuation devices locked. For the secondary motion, theoretical predictions are compared with experimental measurements obtained on a physical specimen tested at the RPL of the University of Salerno (see Sect. 3.1.2).

It is worth emphasizing that, in the systems considered here, stiffness arises solely from the elasticity of bars and cables, whereas in the configurations studied in (Miranda et al., 2020) the mechanical characteristics of the external actuators play a more prominent role. In the structures examined in what follows, deformation is primarily associated with cable stretching, since the cables are markedly more compliant than the bars.

Let $\mathbf{q}$ collect the free displacement components of the unconstrained nodes of $\mathcal{P}$ with respect to a chosen reference configuration. Assuming that such nodes are not directly loaded by external forces, the corresponding equilibrium conditions read

$$g_r(\mathbf{q}) \;=\; \sum_{m=1}^{M} k_m \,(\ell_m(\mathbf{q}) - \bar{\ell}_m)\, \frac{\partial \ell_m}{\partial q_r} \;=\; 0 \tag{3.1}$$

where k_m is the stiffness parameter of the m-th bar or cable in $\mathcal{P}$ ($m = 1, \ldots, M$), $\bar{\ell}_m$ is its rest length, ℓ_m is its current length, and q_r denotes the r-th component of $\mathbf{q}$ ($r = 1, \ldots, Q$) (Fraternali et al., 2015a). A deformation history is generated by prescribing the evolution in time of a subvector $\mathbf{q}_p$ of $\mathbf{q}$, namely by imposing $\mathbf{q}_p = \mathbf{u}(t)$. The resulting equilibrium problem can be cast in the *extended system of equations* form (Fraternali et al., 2015b)

$$\left\{ \begin{array}{c} \mathbf{g}(\mathbf{q}(t)) \\ \mathbf{q}_p - \mathbf{u}(t) \end{array} \right\} \;=\; \mathbf{0} \tag{3.2}$$

where $\mathbf{g}$ collects the residuals $g_1, \ldots, g_Q$.

It is convenient to discretize the evolution into time instants $t_1, \ldots, t_S$. For the incremental step $t_s \to t_{s+1}$, let $\bar{\mathbf{q}}$ be an initial estimate of $\mathbf{q}(t_{s+1})$ satisfying

$\bar{\mathbf{q}}_p = \mathbf{u}(t_{s+1})$, and define $\bar{\mathbf{g}} = \mathbf{g}(\bar{\mathbf{q}})$. We also consider the complementary subvectors $\mathbf{q}^a$ and $\mathbf{g}^a$, obtained by removing the prescribed components $\bar{\mathbf{q}}_p$ and $\bar{\mathbf{g}}_p$ from $\bar{\mathbf{q}}$ and $\bar{\mathbf{g}}$, respectively. A Newton–Raphson correction $\boldsymbol{\Delta}\mathbf{q}^a$ is then computed by solving

$$\mathbf{K}^{T,aa}\ \boldsymbol{\Delta}\mathbf{q}^a\ =\ -\mathbf{g}^a \tag{3.3}$$

where $\mathbf{K}^{T,aa}$ is the submatrix of the *tangent stiffness matrix* with entries $K^T_{ij} = \partial g_i/\partial q_j$, associated with $\mathbf{g}^a$ and $\mathbf{q}^a$. Iterations of (3.3) are performed until $\|\boldsymbol{\Delta}\mathbf{q}^a\|$ becomes smaller than $10^{-6}\,\ell_{0_{min}}$, where $\ell_{0_{min}}$ denotes the minimum member length among those forming $\mathcal{P}$ in the configuration at $t = 0$.

3.1.1 Stabilization of the primary motion

We adopt, as reference state, the fully folded placement ($\varepsilon = \varepsilon_{\max}$) of a right macro-triangle $\mathcal{P} \equiv \mathcal{T}$, and study a deformation process driven by a prescribed history $u(t)$ for the displacement of $\mathbf{x}_0$ along the $\mathbf{e}_3$ direction (Fig. 3.1). In the special case $\alpha = \pi/2$ (right macro-triangle; cf. Fig. 2.8), we assume that the evolution takes place under the constraints that $\mathbf{x}_1$ slides along the $\mathbf{e}_1$ axis, $\mathbf{x}_3$ slides along the $\mathbf{e}_2$ axis, and the rest lengths of both the opening and closing cable families remain constant (Fig. 2.6).

We begin by deriving a linear approximation of the response of $\mathcal{P}$ by evaluating Eqn. (3.3) at the first time increment ($t = t_1$). We then investigate the geometrically nonlinear behavior of $\mathcal{P}$ by means of a Mathematica® implementation of the path-following strategy introduced in the preceding section.

Because the imposed motion corresponds to a downward travel of $\mathbf{x}_0$, the opening cables are put in tension throughout the considered deformation path. The closing cables, instead, contribute only if an initial prestrain $p_0 = (\ell_0 - \bar{\ell})/\bar{\ell}$ is assigned (through the perimeter bus cable) to both opening and closing families. Once activated, the closing cables remain taut only up to the stage where they lose tension as u increases. In the above definition, ℓ_0 and $\bar{\ell}$ are, respectively, the cable length in the reference configuration and its rest length. If one considers the opposite scenario—starting from the flat configuration and moving $\mathbf{x}_0$ upward—the mechanical roles of opening and closing cables interchange. In the model, the opening cables link nodes $\mathbf{x}_1$ and $\mathbf{x}_3$ to a node $\mathbf{x}_4$ held fixed at the projection of $\mathbf{x}_0$ on the $\mathbf{e}_1$–$\mathbf{e}_2$ plane (Fig. 3.1).

The closing cables connect $\mathbf{x}_1$ and $\mathbf{x}_3$ to nodes $\mathbf{x}_5$ and $\mathbf{x}_6$, which are fixed at the vertices of $\mathcal{P}$ lying on the global x and y axes in the fully open configuration.

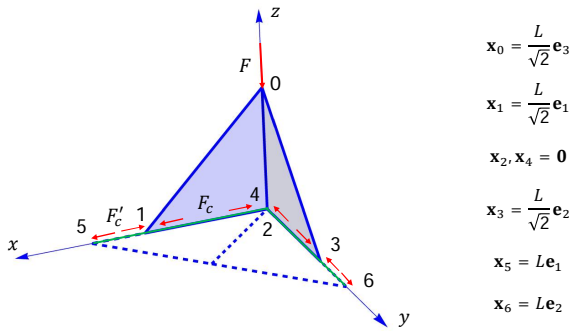

Figure 3.1: Schematic of the mechanical model adopted to investigate stabilization of the primary folding motion (reproduced from Fraternali et al., 2024b under the license CC BY-NC-ND 4.0).

Imposing the cable prestrain p_0 produces the pretension forces F_c and F_c' in such members (Fig. 3.1), namely

$$F_{c_p} \;=\; F'_{c_p} \;=\; (EA)_c \; p_0 \tag{3.4}$$

where $(EA)_c$ denotes the axial stiffness of the cable material (Young modulus times cross-sectional area). The bar elements depicted in Fig. 3.1 represent the supporting substructure of the micro-triangle plates belonging to $\mathcal{P}$, and are characterized by axial stiffness $(EA)_b$. Let u_{x_i}, u_{y_i}, u_{z_i} be the Cartesian components of the displacement of node $\mathbf{x}_i$ measured from the reference placement in Fig. 3.1. The set of nonvanishing kinematic variables is collected in $\mathbf{q} = \{u_{z_0}, u_{x_1}, u_{x_2}, u_{y_2}, u_{z_2}, u_{y_3}\}$.

3.1.1.1 Linearized response

We focus first on the case $p_0 = 0$ (hence $F_c' = 0$). In that setting, the equilibrium conditions for the system in Fig. 3.1, written along the directions associated with the entries of $\mathbf{q}$, can be expressed as

$$\mathbf{g} = \; \mathbf{A}\mathbf{f} - \mathbf{w} = \mathbf{0} \tag{3.5}$$

where $\mathbf{f}$ collects the axial forces in members 1–4, 3–4, 0–1, 1–2, 0–2, 0–3, 2–3 (positive in tension), $\mathbf{w}$ is the vector of applied nodal loads, and $\mathbf{A}$ is the

equilibrium matrix

$$\mathbf{A} = \begin{pmatrix} 0 & 0 & \frac{1}{\sqrt{2}} & 0 & 1 & \frac{1}{\sqrt{2}} & 0 \\ \frac{1}{\sqrt{2}} & 0 & \frac{1}{\sqrt{2}} & 1 & 0 & 0 & 0 \\ 0 & 0 & 0 & -1 & 0 & 0 & 0 \\ 0 & 0 & 0 & 0 & 0 & 0 & -1 \\ 0 & 0 & 0 & 0 & -1 & 0 & 0 \\ 0 & \frac{1}{\sqrt{2}} & 0 & 0 & 0 & \frac{1}{\sqrt{2}} & 1 \end{pmatrix} \tag{3.6}$$

Introducing linear axial constitutive relations for cables and bars yields

$$\begin{aligned} f_1 &= k_c \left(||(\mathbf{x}_1 + q_2\ \mathbf{e}_1) - \mathbf{x}_4|| - \bar{\ell}_{1,4} \right) \\ f_2 &= k_c \left(||(\mathbf{x}_3 + q_6\ \mathbf{e}_2) - \mathbf{x}_4|| - \bar{\ell}_{3,4} \right) \\ f_3 &= k_b \left(||(\mathbf{x}_0 + q_1\ \mathbf{e}_3) - (\mathbf{x}_1 + q_2\ \mathbf{e}_1)|| - \bar{\ell}_{0,1} \right) \\ f_4 &= k_b \left(||(\mathbf{x}_1 + q_2\ \mathbf{e}_1) - (\mathbf{x}_2 + q_3\ \mathbf{e}_1 + q_4\ \mathbf{e}_2 + q_5\ \mathbf{e}_3)|| - \bar{\ell}_{1,2} \right) \\ f_5 &= k_b \left(||(\mathbf{x}_0 + q_1\ \mathbf{e}_3) - (\mathbf{x}_2 + q_3\ \mathbf{e}_1 + q_4\ \mathbf{e}_2 + q_5\ \mathbf{e}_3)|| - \bar{\ell}_{0,2} \right) \\ f_6 &= k_b \left(||(\mathbf{x}_0 + q_1\ \mathbf{e}_3) - (\mathbf{x}_3 + q_6\ \mathbf{e}_2)|| - \bar{\ell}_{0,3} \right) \\ f_7 &= k_b \left(||(\mathbf{x}_2 + q_3\ \mathbf{e}_1 + q_4\ \mathbf{e}_2 + q_5\ \mathbf{e}_3) - (\mathbf{x}_3 + q_6\ \mathbf{e}_2)|| - \bar{\ell}_{2,3} \right) \end{aligned} \tag{3.7}$$

where $k_c = (EA)_c/\bar{\ell}_c$ and $k_b = (EA)_b/\bar{\ell}_b$, with $\bar{\ell}_c$ and $\bar{\ell}_b$ denoting the rest length of the specific cable or bar considered. Substituting Eqns. (3.7) into (3.5) allows one to assemble the tangent stiffness matrix $\mathbf{K}^{T,0} = \{\partial g_i/\partial q_j\}$ at the reference configuration of Fig. 3.1, obtaining

$$\mathbf{K}^{T,0} = \frac{1}{L} \begin{pmatrix} \left(1+\sqrt{2}\right) B & \frac{B}{2} & 0 & 0 & -\sqrt{2}B & \frac{B}{2} \\ \frac{B}{2} & \left(\frac{1}{2}+\sqrt{2}\right) B + \sqrt{2}C & -\sqrt{2}B & 0 & 0 & 0 \\ 0 & -\sqrt{2}B & \sqrt{2}B & 0 & 0 & 0 \\ 0 & 0 & 0 & \sqrt{2}B & 0 & -\sqrt{2}B \\ -\sqrt{2}B & 0 & 0 & 0 & \sqrt{2}B & 0 \\ \frac{B}{2} & 0 & 0 & -\sqrt{2}B & 0 & \left(\frac{1}{2}+\sqrt{2}\right) B + \sqrt{2}C \end{pmatrix} \tag{3.8}$$

with $B = (EA)_b$ and $C = (EA)_c$. Under the small-displacement assumption, the equilibrium statement (3.5) reduces to the linear elastic problem

$$\mathbf{K}^{T,0}\ \mathbf{q}\ =\ \mathbf{w} \tag{3.9}$$

In the idealized limit of inextensible bars, $B \to \infty$, and for a single downward vertical force F applied at node $\mathbf{x}_0$, one obtains

$$\mathbf{q}^0 = \frac{F\ L}{2\sqrt{2}C}\ \{-1, 1, 1, 1, -1, 1\} \tag{3.10}$$

The same approximation predicts that the tension in each opening cable equals

$$F_c^0 \;=\; \frac{F}{2} \tag{3.11}$$

Let $F_{c,f}$ denote the ultimate tensile load of the cables. If Eqn. (3.11) were to hold throughout the motion, cable rupture would be expected when F reaches $F_f = 2F_{c,f}$. As shown in the next subsection, however, the ratio F_c/F increases substantially as the structure moves away from the reference placement, so that failure may occur for values of F well below $2F_{c,f}$.

3.1.1.2 Response in the large displacement regime

We now turn to the large-displacement behavior of the macro-triangle $\mathcal{P}$ in Fig. 3.1, solved via the displacement-control continuation method outlined in Sect. 3.1. The prescribed subvector is taken as $\mathbf{q}_p = \{u_p\}$ with $u_p \equiv u_{z_0}$, and u_p is imposed to evolve linearly in time according to $u(t)$, from $u = 0$ at the initial step to $u = u_{max} = \sqrt{\varepsilon_{\max}(2-\varepsilon_{\max})}\,L = L/\sqrt{2}$ at the final step (cf. Sect. 2.4). The numerical model adopts geometry and member dimensions consistent with a simplified version of the small-scale demonstrator discussed in Sect. 2.2: $\mathcal{P}$ is composed of two isosceles right micro-triangles with hypotenuse $L = 183$ mm. This reduced model is later reused as a building block for the quadrilateral dynamics analyzed in Sect. 3.2. The opening and closing cables associated with $\mathcal{P}$ are modeled as monofilament nylon line with diameter 0.40 mm, Young modulus 1.0 MPa, and breaking force $F_{c,f} = 21.57$ N. The bar framework is steel with Young modulus 210 GPa and rectangular section 3 mm $\times$ 5 mm.

Figure 3.2(a) presents computed F–u curves for different values of the pre-strain p_0 (constructed using a deformation history discretized into 5000 steps). The external force F is identified with the residual component g_p dual to u_p in Eqn. (3.1). In Fig. 3.2(a), forces are normalized by $F_{c,f}$ and displacements by the stroke u_{max}. The dashed segments labelled (ii) correspond to a hypothetical continuation beyond cable rupture (cable forces larger than $F_{c,f}$), whereas the solid portions labelled (i) represent feasible response branches (cable forces not exceeding $F_{c,f}$). Panel (b) of Fig. 3.2 illustrates a representative deformed shape, and panel (c) reports the evolution of the ratio F_c/F for u/u_{max} between 0 and 0.8.

The family of curves in Fig. 3.2(a) shows a progressive reduction of the tangent stiffness as u increases (i.e., the F–u slope decreases in magnitude). If

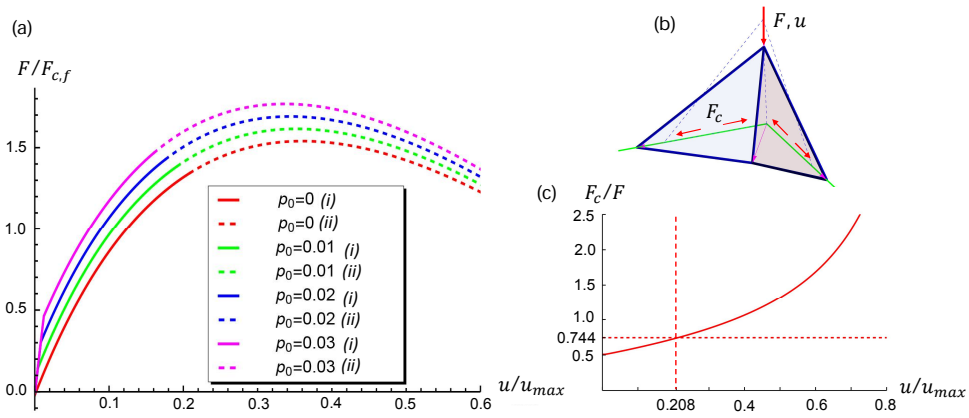

Figure 3.2: (a) Numerical curves of $F/F_{c,f}$ versus u/u_{umax} for stabilization of the primary folding motion in a reduced-scale macro-triangle, for different cable prestrains p_0. Solid portions (i) correspond to admissible branches with cable tension below $F_{c,f}$; dashed portions (ii) extend beyond cable rupture and are shown only for reference. (b) Example of a deformed configuration. (c) Evolution of the ratio F_c/F with the vertical displacement of the top node, for $p_0 = 0$ (reproduced from Fraternali et al., 2024b under the license CC BY-NC-ND 4.0).

the cables could sustain sufficiently large tensile forces, such softening would ultimately culminate in a limit-point instability (Budiansky, 1974). The corresponding load level is denoted F_l. The computations in Fig. 3.2(a) locate the limit point at a displacement $u = u_l$ ranging from $0.34\,u_{max}$ for $p_0 = 0$ to $0.36\,u_{max}$ for $p_0 = 0.03$, indicating that the instability would occur after roughly one third of the available stroke of $\mathbf{x}_0$. The same plots also show a modest upward shift of the response for increasing p_0, which is attributable to stiff initial branches near $u = 0$ caused by the early engagement of closing cables when $p_0 > 0$. For the considered mock-up, the failure load is found to be $F_f = 1.343\,F_{c,f}$ at $u = 0.208\,u_{max}$ for $p_0 = 0$, and $F_f = 1.46\,F_{c,f}$ at $u = 0.160\,u_{max}$ for $p_0 = 3\%$. In the same simulations, the limit-point value becomes $F_l = 1.540\,F_{c,f}$ for $p_0 = 0$ and $F_l = 1.768\,F_{c,f}$ for $p_0 = 3\%$. A key outcome is that $F_f/F_{c,f}$ is far below the factor 2 suggested by the linear estimate of the previous subsection. For $p_0 = 0$, Fig. 3.2(c) shows that F_c/F rises well above 0.5 immediately after leaving $u = 0$, reaching 0.744 at $u = 0.208\,u_{max}$.

If the external actions applied to $\mathcal{P}$ (typically wind-induced loads (Miranda

et al., 2020)) are expected to generate cable forces larger than F_f, protective measures should be implemented for the module. One viable option is to introduce motion stoppers (e.g., spring-based end stops with suitable rest lengths) placed at the ends of the diagonal sliding tracks depicted in Fig. 2.6.

3.1.2 Stabilization of the secondary motion

A combined numerical–experimental investigation was carried out to assess the stabilization mechanisms associated with the secondary folding motion of a representative micro-triangle. The analyzed element reproduces the essential geometric and mechanical characteristics of the micro-triangles employed in the demonstrative prototype discussed in Sect. 2.2. Numerical predictions were systematically compared with experimental measurements obtained at the Rapid Prototyping Laboratory of the University of Salerno.

3.1.2.1 Physical model and experimental setup

The experimental campaign focused on the micro-triangle illustrated in Fig. 3.3, whose geometry is defined—according to the notation introduced in Sect. 2.4—by the parameters $a = 60$ mm, $b = 0$ mm, $c = 41.05$ mm, and $L/\sqrt{2} = 116.14$ mm. A physical specimen was manufactured with this geometry. The supporting frame consisted of bars with rectangular cross section 3 mm $\times$ 5 mm, while the scissor mechanism employed pins with 2.8 mm $\times$ 1.5 mm cross section. These structural components were produced by Shapeways® using Matte Black Steel, characterized by a Young modulus of 210 GPa. The foldable plate was fabricated in gray ABS with a thickness of 3 mm at the RPL facility. ABS was selected in place of steel to reduce inertial effects, which are neglected in the numerical simulations discussed below. The scissor pins were linked to a closed-loop bus cable made of nylon wire with diameter 0.4 mm, identical to that adopted for the primary-motion experiments.

The frame was rigidly fixed to an optical bench, and quasi-static loading tests were performed to characterize the stiffness of the system once stabilized. Stabilization was achieved by locking the rest length of the bus cable, which was anchored to the supporting frame. The quantity monitored during testing was the change Δd in the distance d between nodes $\mathbf{y}_2$ and $\mathbf{x}_2$ (Fig. 3.3), induced by an external load progressively closing the foldable plate. Prior to loading, the plate was set in a partially folded configuration forming a 52° angle with the horizontal plane. The corresponding initial distance is

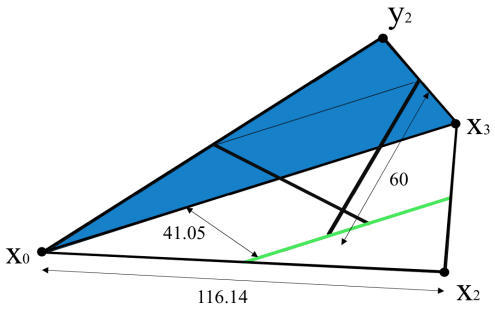

Figure 3.3: Geometry of the tested sample of a micro-triangle (dimensions in mm) (reproduced from Fraternali et al., 2024b under the license CC BY-NC-ND 4.0).

denoted by d_0. Prestress was introduced in the base cables by attaching them to external baskets carrying calibrated masses. Each cable was connected to its prestress basket via a small pyramid-shaped steel linkage composed of 1 mm diameter bars (Fig. 3.4(a)). Two prestress levels were examined, namely $F_{c,p} = 250$ gf and $F_{c,p} = 500$ gf. When normalized by the cable breaking force $F_{c,f} = 21.57$ N, these prestress values correspond to $F_{c,p} = 0.114\, F_{c,f}$ and $F_{c,p} = 0.227\, F_{c,f}$. After prestressing, the cable lengths were mechanically locked and the prestress baskets removed (Fig. 3.4(b)). Subsequently, node $\mathbf{y}_2$ was subjected to vertical loading through a loading basket connected by a 0.76 mm PowerPro® braided Spectra fiber routed through the frame (Fig. 3.4). The applied weight generated a force F transmitted directly to $\mathbf{y}_2$. The displacement $\Delta d = d_0 - d$ was measured by tracking the vertical motion of a reference plate attached to the loading basket using a laser displacement sensor (Fig. 3.4(a,b)). Loads were applied incrementally in steps of 20 g or 50 g, and the displacement was recorded after each increment. An image of the specimen during testing is provided in Fig. 3.4(c).

3.1.2.2 Mechanical model and force-displacement response

The analytical description of the experiment relies on the mechanical model depicted in Fig. 3.5(a), which was developed to reproduce the response of the tested specimen introduced in Sect. 3.1.2.1. Panels (b) and (c) of the same figure show two representative configurations of the physical model. The vectors $\mathbf{x}_i$ and $\mathbf{y}_i$ denote the nodal positions in the reference and deformed

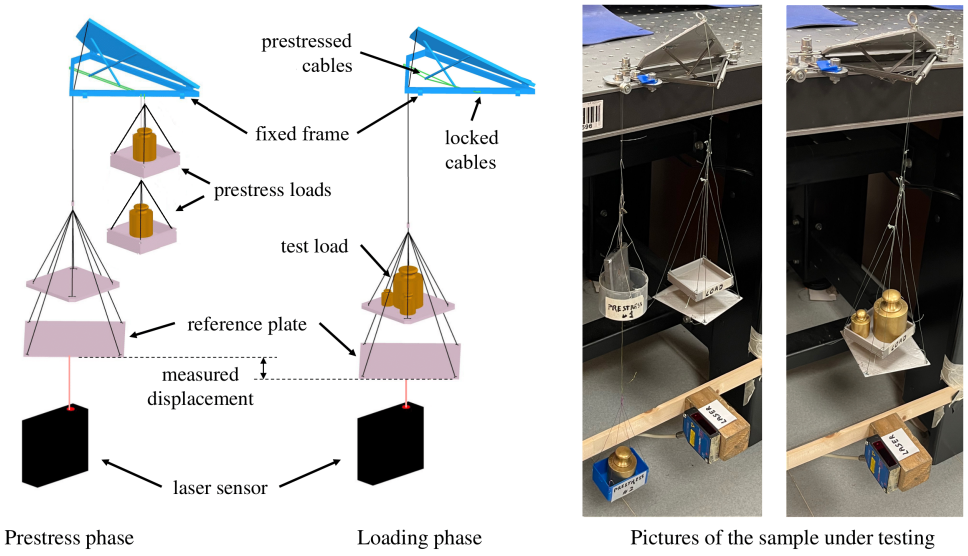

Figure 3.4: Illustrative scheme of the loading test carried out on a reduced scale micro-triangle (a-b), and pictures of the physical sample under testing (c) (reproduced from Fraternali et al., 2024b under the license CC BY-NC-ND 4.0).

configurations, respectively, for the nine-node system shown in Fig. 3.5(a). Nodes 0 through 4 remain fixed during the deformation process, while nodes 5, 6, and 7 undergo a rigid rotation about the x-axis by an angle θ, decreasing from 52° to zero. This kinematic evolution is described by

$$\begin{pmatrix} y_{x_i} \\ y_{y_i} \\ y_{z_i} \end{pmatrix} = \begin{pmatrix} 1 & 0 & 0 \\ 0 & \cos\theta & -\sin\theta \\ 0 & \sin\theta & \cos\theta \end{pmatrix} \begin{pmatrix} X_{x_i} \\ X_{y_i} \\ X_{z_i} \end{pmatrix}, \qquad (i = 5, 6, 7) \qquad (3.12)$$

where X_{x_i}, X_{y_i}, and X_{z_i} denote nodal coordinates in the fully closed configuration. The displacement vector $\mathbf{q}$ collects the nonzero displacement components of nodes 5 through 9. Prescribed displacements associated with the folding motion of nodes 5–7 define the subvector $\mathbf{q}_p$, while the unknown displacement components of nodes 8 and 9 are grouped in $\mathbf{q}^a = \{u_{x_8}, u_{y_8}, u_{z_8}, u_{x_9}, u_{y_9}, u_{z_9}\}$. The deformable elements of the system consist of cables 8–4, 8–3, 9–3, 9–4 and bars 6–9 and 7–8; all remaining components either undergo rigid-body motion or remain stationary. Although cables 8–4 and 8–3 coincide with cables 9–4

and 9–3 in the reference configuration, they are treated as distinct elements and deform differently. In the physical prototype, these cables are slightly offset in the transverse direction, as shown in Fig. 3.5(b,c).

The equilibrium of nodes 8 and 9 yields the governing equations for $\mathbf{q}^a$:

$$\mathbf{g}_8 = f_{3,8}\frac{\mathbf{y}_3 - \mathbf{y}_8}{\ell_{3,8}} + f_{0,8}\frac{\mathbf{y}_0 - \mathbf{y}_8}{\ell_{0,8}} + f_{7,8}\frac{\mathbf{y}_7 - \mathbf{y}_8}{\ell_{7,8}} = \mathbf{0}, \tag{3.13}$$

$$\mathbf{g}_9 = f_{0,9}\frac{\mathbf{y}_0 - \mathbf{y}_9}{\ell_{0,9}} + f_{3,9}\frac{\mathbf{y}_3 - \mathbf{y}_9}{\ell_{3,9}} + f_{6,9}\frac{\mathbf{y}_6 - \mathbf{y}_9}{\ell_{6,9}} = \mathbf{0}, \tag{3.14}$$

which may be compactly written as

$$\mathbf{g} = \left\{ \begin{array}{c} \mathbf{g}_8 \\ \mathbf{g}_9 \end{array} \right\} = \mathbf{0}. \tag{3.15}$$

Axial forces are related to elongations through linear elastic laws $f_{i,j} = k_{i,j}(||\mathbf{y}_i - \mathbf{y}_j|| - \bar{\ell}_{i,j})$, with stiffnesses $k_{i,j} = (EA)_c/\bar{\ell}_c$ for cables and $k_{i,j} = (EA)_b/\bar{\ell}_b$ for bars. By combining these relations with Eqns. (3.12), the residual vector $\mathbf{g}$ is expressed as a nonlinear function of $\mathbf{q}$. The resulting equilibrium equations (3.15) are solved via the continuation strategy described in Sect. 3.1, prescribing a stepwise reduction of θ from 52° to zero over 100 equal increments. At each increment, the force F applied at node 5 is obtained by enforcing vanishing moment equilibrium of micro-triangle $\overset{\triangle}{015}$ about the 0–1 support axis:

$$\left((\mathbf{y}_6 - \mathbf{y}_0) \times f_{6,9}\frac{\mathbf{y}_6 - \mathbf{y}_9}{\ell_{6,9}} + (\mathbf{y}_7 - \mathbf{y}_0) \times f_{7,8}\frac{\mathbf{y}_7 - \mathbf{y}_8}{\ell_{7,8}} - (\mathbf{y}_5 - \mathbf{y}_0) \times F\frac{\mathbf{y}_5 - \mathbf{y}_2}{\ell_{5,2}} \right) \cdot \mathbf{e}_1 = 0. \tag{3.16}$$

Figure 3.6(a) compares numerical and experimental curves of $F/F_{c,f}$ versus $\Delta d/d_0$ for the examined prestress levels $F_{p,c}$. As for the primary-motion analysis, dashed segments indicate portions of the response exceeding the cable strength. Panel (b) shows a deformed configuration, while panel (c) reports the evolution of F_c/F with $\Delta d/d_0$ for $F_p = 0.114\, F_{c,f}$. The response is characterized by an initial stiffening regime followed by a softening branch.

The numerical simulations predict a limit-point instability at the end of the softening phase, in qualitative agreement with the behavior observed for the

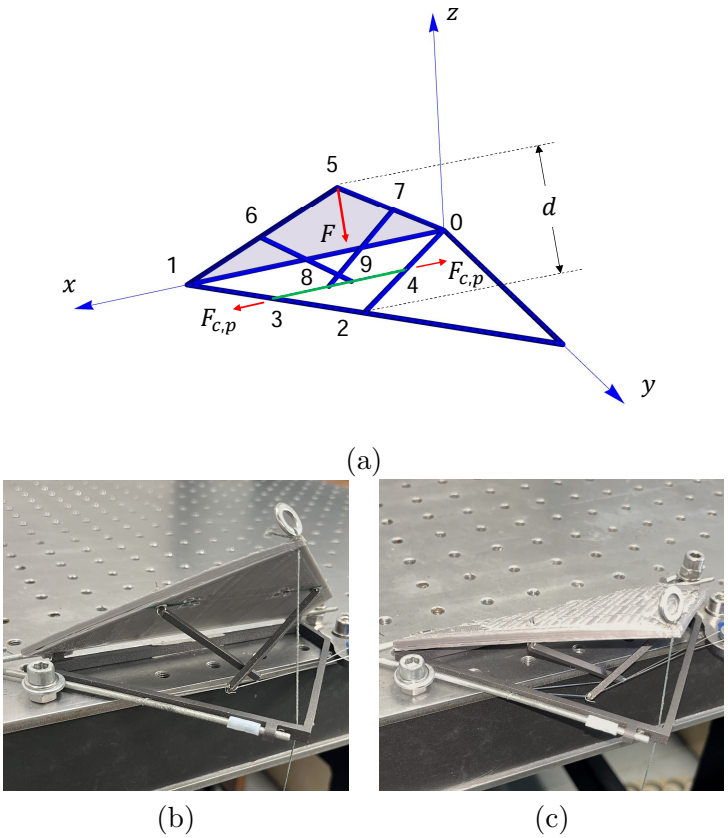

Figure 3.5: Illustration of the mechanical and physical models employed for the study of the stabilization of the secondary folding motion. (a) Reference configuration of the mechanical model. (b) Close-up of the physical prototype in the reference configuration. (c) Deformed configuration during testing (reproduced from Fraternali et al., 2024b under the license CC BY-NC-ND 4.0).

primary motion. In the present case, this instability is reached for $\Delta d/d_0 \simeq 1$ (i.e., $\theta \simeq 0$). The correspondence between simulations and experiments in Fig. 3.6(a) is generally good. For $F_p = 0.114\, F_{c,f}$, the experimental curve terminates at the failure load $F_f = 0.438\, F_{c,f}$, reached at approximately 68% of the full stroke. For $F_p = 0.227\, F_{c,f}$, the numerical model predicts $F_f = 0.432\, F_{c,f}$ at about 61% of the stroke. Finally, Fig. 3.6(c) shows that the ratio F_c/F is initially large at small displacements, and subsequently decreases to

values between 3.45 and 3.60 for Δd between 50% and 80% of d_0, assuming $F_p = 0.113\, F_{c,f}$.

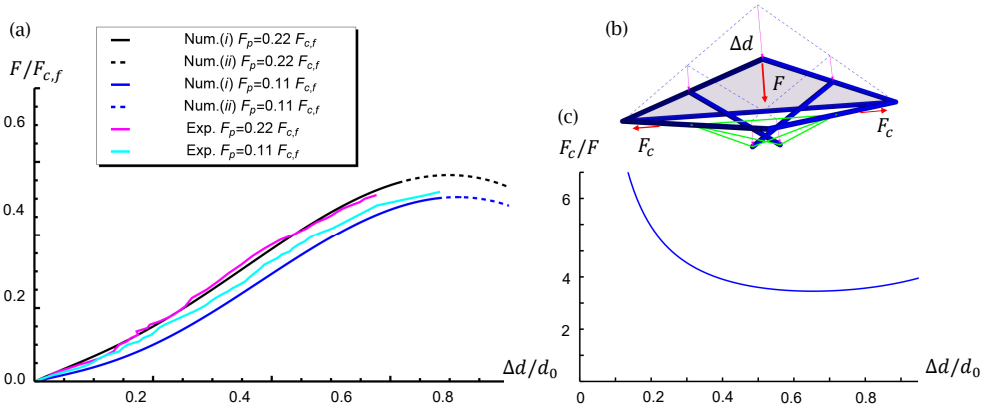

Figure 3.6: (a) Comparison between numerical predictions and experimental measurements of the force–displacement response associated with the stabilization of the secondary folding motion, for different prestress levels F_p. (b) Deformed configuration. (c) Evolution of the ratio F_c/F as a function of $\Delta d/d_0$, for $F_p = 0.113\, F_{c,f}$ (reproduced from Fraternali et al., 2024b under the license CC BY-NC-ND 4.0).

In scenarios involving extreme actions, such as intense wind events capable of generating forces beyond the cable failure threshold, protective strategies may be adopted by driving the system toward a closed configuration, similarly to the automatic retraction mechanisms employed in wind-sensitive awnings (Goodman and Meier, 2013).

3.2 Dynamic response and wind loading

We next investigate the vibration behavior of the quadrilateral assembly depicted in Fig. 3.7, considering the solar eye in an intermediate (semi-closed) placement characterized by $\varepsilon = 0.5\, \varepsilon_{\max}$. The analysis adopts this configuration as the reference state for assessing the consequences of upwind excitation, namely wind acting orthogonally to the module base plane (hence normal to a façade on which solar eyes are installed). Such a choice is motivated by exposure considerations: compared with the fully folded and fully flat states,

the semi-closed arrangement presents a larger effective surface to the incoming flow. Indeed, the fully open (fully folded) state examined in Sect. 3.1.1 yields a negligible—ideally vanishing—projected area under upwind loading, whereas the fully closed configuration benefits from shielding by the surrounding frame, which mitigates wind-driven oscillations (see Figs. 2.6–2.7). Under high or moderately high wind intensities, we assume that the secondary folding mechanism is not actuated, consistently with the remarks given at the end of the preceding section.

In upwind conditions, the load tends to push the central node 0 of the scheme in Fig. 3.7 downward, i.e., it promotes a negative displacement component along the z-axis. Accordingly, the adopted mechanical idealization includes only the opening cable set 1–4, 3–4, 6–4, 8–4, while the closing cables are taken as inactive because no prestress is introduced. Conversely, a downwind scenario would require the complementary modeling assumption (closing cables active and opening cables slack), still under the simplifying hypothesis of zero prestress.

The position vectors of the vertices of macro-triangle 0–1–2–3 are prescribed as

$$\begin{aligned}
\mathbf{x}_0 &= \left\{0, 0, \frac{1}{2}\sqrt{\frac{5}{2} - \sqrt{2}}L\right\} \\
\mathbf{x}_1 &= \left\{\frac{1}{4}\left(2 + \sqrt{2}\right)L, 0, 0\right\} \\
\mathbf{x}_2 &= \left\{\frac{L}{4 + \sqrt{2}}, \frac{L}{4 + \sqrt{2}}, -\frac{\sqrt{5 - 2\sqrt{2}}L}{8 + 2\sqrt{2}}\right\} \\
\mathbf{x}_3 &= \left\{0, \frac{1}{4}\left(2 + \sqrt{2}\right)L, 0\right\}
\end{aligned} \tag{3.17}$$

and these expressions can be extended in a straightforward manner to define the coordinates of the remaining nodes in Fig. 3.7. Node 4 coincides with the origin of the global Cartesian frame $\{x, y, z\}$ and is assumed fixed.

The objective is to characterize the small-amplitude, wind-induced oscillations about the adopted reference configuration of Fig. 3.7. In the present model, the set of free kinematic variables $\mathbf{q}$ includes: the vertical displacement of node 0; the x-direction displacements of nodes 1 and 6; the y-direction displacements of nodes 3 and 8; and the three Cartesian displacement components of nodes 2, 5, 7, and 9, yielding 17 generalized displacement components over-

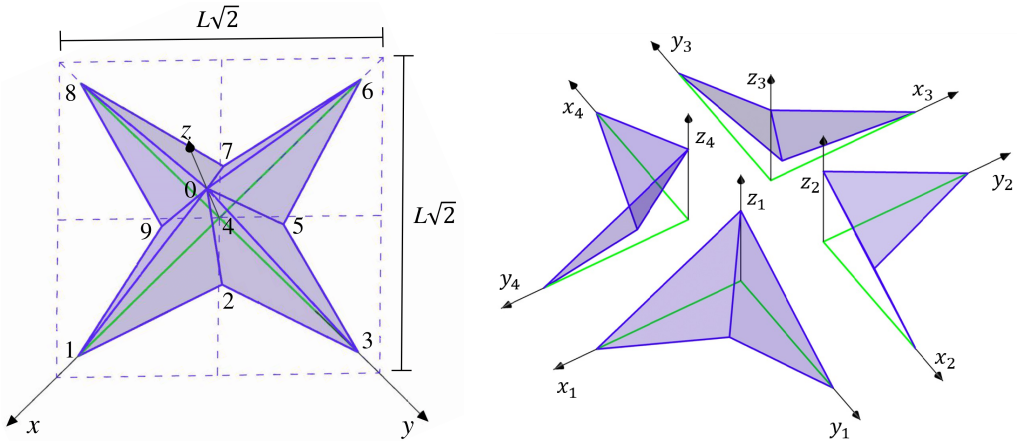

Figure 3.7: (a) Three-dimensional view of the mechanical model of a quadrilateral system. (b) Disassembling of the system into four macro-triangles (reproduced from Fraternali et al., 2024b under the license CC BY-NC-ND 4.0).

all. The tangent stiffness operator at the reference configuration, denoted by $\mathbf{K}^{T,0}$, is obtained by assembling the element tangent stiffness matrices $\mathbf{K}^{T,e}$ corresponding to the four macro-triangles forming the module (Fig. 3.7). Let $\mathbf{q}^1 = \{u_{z_0}, u_{x_1}, u_{x_2}, u_{y_2}, u_{z_2}, u_{y_3}\}$ collect the degrees of freedom associated with the 0–1–2–3 macro-triangle. By repeating the same linearization strategy used in Sect. 3.1.1.1, one finds that the element tangent stiffness takes the form

$$\mathbf{K}^{T,1} = \frac{1}{L}\begin{pmatrix} k_{11} & k_{12} & k_{13} & k_{14} & k_{15} & k_{16} \\ & k_{22} & k_{23} & k_{24} & k_{25} & k_{26} \\ & & k_{33} & k_{34} & k_{35} & k_{36} \\ & Sym & & k_{44} & k_{45} & k_{46} \\ & & & & k_{55} & k_{56} \\ & & & & & k_{66} \end{pmatrix}, \tag{3.18}$$

with coefficients

$$
\begin{aligned}
k_{11} &= \frac{1}{196}\left(309 + 26\sqrt{2}\right) B \\
k_{12} = k_{16} &= \frac{1}{8}\sqrt{7 + 4\sqrt{2}}B \\
k_{13} = k_{14} &= \frac{1}{49}\sqrt{430 - 104\sqrt{2}}B \\
k_{15} &= -\frac{1}{49}\left(16 + 31\sqrt{2}\right) B \\
k_{22} = k_{66} &= \frac{1}{392}\left(363 + 296\sqrt{2}\right) B - \left(2\sqrt{2} - 4\right) C \\
k_{23} = k_{46} &= -\frac{1}{196}\left(108 + 99\sqrt{2}\right) B \\
k_{24} = k_{36} &= \frac{1}{98}\left(30 + 3\sqrt{2}\right) B \\
k_{25} = k_{56} &= -\frac{1}{392}\sqrt{645 - 156\sqrt{2}}B \\
k_{26} &= 0 \\
k_{33} = k_{44} &= \frac{1}{196}\left(44 + 171\sqrt{2}\right) B \\
k_{34} &= \frac{1}{49}\left(6\sqrt{2} - 38\right) B \\
k_{35} = k_{45} &= -\frac{1}{192}\sqrt{2351 - 1328\sqrt{2}}B \\
k_{55} &= \frac{1}{98}\left(123\sqrt{2} - 44\right) B
\end{aligned}
\tag{3.19}
$$

where B and C retain the meaning assigned in Sect. 3.1.1.1. The remaining three element matrices are obtained from $\mathbf{K}^{T,1}$ by expressing the same coefficients in the corresponding local frames $\{x_i, y_i, z_i\}$ associated with each macro-triangle (Fig. 3.7(b)).

To define inertia, let m denote the mass assigned to a micro-triangle. A lumped-mass idealization is adopted by distributing such mass to the triangle

vertices, which produces, for a generic macro-triangle, the element mass matrix

$$\mathbf{M}^e = \frac{1}{3}\, m \begin{pmatrix} 2 & 0 & 0 & 0 & 0 & 0 \\ 0 & 1 & 0 & 0 & 0 & 0 \\ 0 & 0 & 2 & 0 & 0 & 0 \\ 0 & 0 & 0 & 2 & 0 & 0 \\ 0 & 0 & 0 & 0 & 2 & 0 \\ 0 & 0 & 0 & 0 & 0 & 1 \end{pmatrix}. \tag{3.20}$$

Assembly of the matrices $\mathbf{M}^e$ yields the global mass matrix $\mathbf{M}$. The free-vibration characteristics of the quadrilateral module in Fig. 3.7 are then obtained through the eigenproblem

$$\left(\mathbf{K}^{T,0} - \Omega^2 \mathbf{M}\right) \mathbf{\Phi} = \mathbf{0}, \tag{3.21}$$

where Ω^2 is diagonal and contains ω_i^2 (squared angular frequencies), and $\mathbf{\Phi}$ collects the corresponding mode shapes; modes are indexed by increasing frequency.

As a representative case, we consider the reduced-scale mock-up with $L = 183$ mm and the mechanical parameters specified in Sect. 3.1.1.2. We also take $m = 0.197$ kg, consistent with the mass of an isosceles right steel micro-triangle of hypotenuse $L = 183$ mm and thickness 3 mm (density 7.85 g/cm^3). The first eigenmode, shown in Fig. 3.8, corresponds to $\nu_1 = 5.77$ Hz and is mainly associated with activation of the primary folding mechanism, opposed by the elastic response of the opening cables (Fig. 3.8). All higher modes are characterized by substantially larger frequencies (e.g., $\nu_2 = 178\,\nu_1$), since they involve deformation of the comparatively stiff steel frames supporting the panels, whereas the first mode primarily mobilizes the compliant nylon cables. Additional higher-order shapes are illustrated. The modal results in Fig. 3.8 were produced via a Mathematica® implementation of Eqn. (3.21) and were checked against finite element computations. For reference, the fundamental transverse frequency of a single pinned nylon cable (mass density 1.14 g/cm^3), with diameter 0.40 mm and length 259 mm, is about 50 Hz when subjected to a tensile force of only 0.1 N. This estimate follows from $\nu_c = 1/(2\sqrt{2}L)\,\sqrt{T/\rho}$, which provides the first mode frequency of a pinned cable of length $\sqrt{2}L$, where T is the axial tension and ρ the linear mass density (Shabana, 1996).

Wind action is inherently unsteady and may induce resonance when the structure (or its components) possesses natural frequencies below approximately 1 Hz (Holmes, 2018). When the relevant frequencies are well above 1

Hz—as for the mock-up analyzed here—wind effects can often be treated as a quasi-static background load. Under this assumption, a static assessment based on international provisions (e.g., Eurocode 1, EN 1991-1-4:2005, European Committee for Standardisation, 2005) becomes appropriate. When resonance cannot be excluded, the corresponding analysis may be developed by extending methodologies devised for large-span roofs to façades equipped with solar eyes (Su et al., 2018). A detailed treatment of such dynamic phenomena, together with cross-wind effects, cladding pressures, and aerodynamic interactions involving the attached solar panels (Wittwer et al., 2022), is outside the scope of the present study and is left for future work.

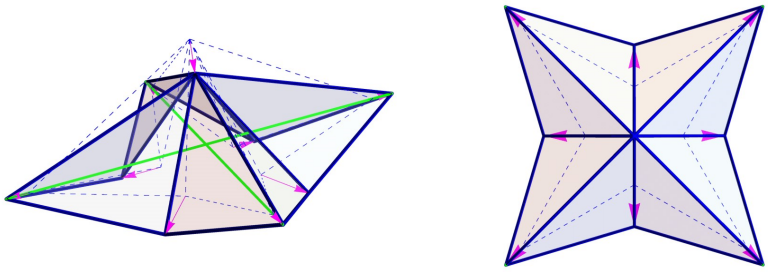

Mode 1: $\nu_1 = 5.77$ Hz

Figure 3.8: First vibration mode of the system in Fig. 3.7 equipped with the dimensions and mechanical properties of the solar eye mock-up (reproduced from Fraternali et al., 2024b under the license CC BY-NC-ND 4.0).

4

Manufacturing of a Quadrilateral Tensegrity-Origami Mock-up

4.1 Components of the a quadrilateral solar module

This chapter outlines the fabrication and integration of a quadrilateral tensegrity–origami solar module. The demonstrator was conceived to corroborate, through a tangible prototype, the geometric and mechanical outcomes discussed in Chapters 2 and 3, and to verify the actuation and control approaches associated with the two distinct folding motions. The mock-up was produced at the Rapid Prototyping Laboratory (RPL) of the University of Salerno, adopting the materials and procedures summarized in the subsequent sections.

Figure 4.1 provides the principal dimensions of the solar eye demonstrator, whereas Figure 4.2 depicts the fully assembled device equipped with five actuation motors. Most of the additively manufactured parts were fabricated with the MakerBot® fused deposition modeling (FDM) printer available at the RPL. The printed components were realized using polylactic acid (PLA) filaments supplied by Fillamentum® (`https://fillamentum.com/`).

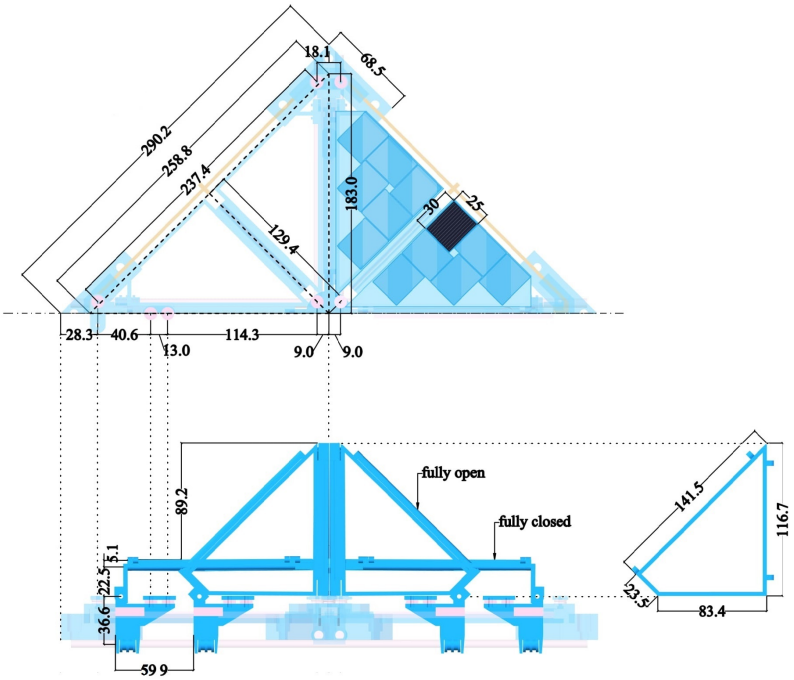

Figure 4.1: Different views with dimensions in mm of the solar eye mock-up (reproduced from Fraternali et al., 2024b under the license CC BY-NC-ND 4.0).

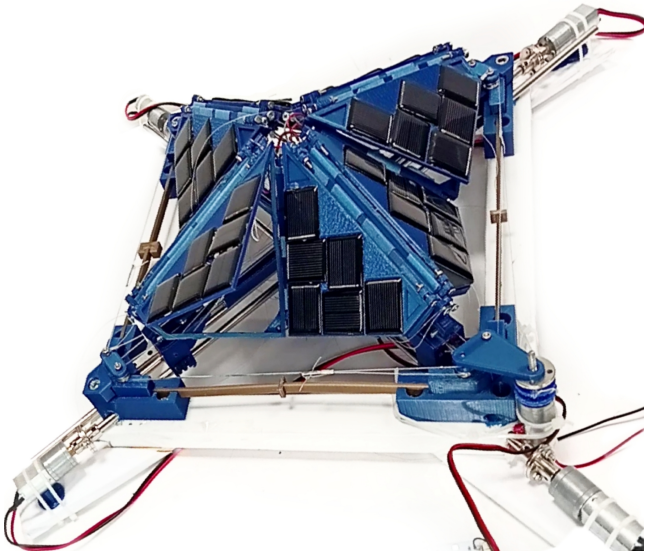

Figure 4.2: Three-dimensional view of the solar eye mock-up equipped with five activation motors (reproduced from Fraternali et al., 2024b under the license CC BY-NC-ND 4.0).

Figs. 4.3 -4.4 collect the component families that, once assembled, constitute the quadrilateral module. For clarity, the module is organized into eight principal subassemblies:

- supporting frame (group #(1), intended to be anchored, for example, to a façade or to a roof substructure);
- two linear tracks and four slider blocks (group #(2)), with the tracks imposing motion of the sliders along the module diagonals;
- four guiding bars associated with the secondary folding kinematics (group #(3)); together with a cable–pulley arrangement governing the primary folding kinematics (group #(4));
- pulley covers (group #(5));
- eight base micro-triangle frames (group #(6)), designed to translate along the diagonals to accommodate the primary folding motion;
- scissor linkages and the corresponding actuation cables for the secondary folding motion (group #(7));

- PV or T panels (group #(8)) to be housed within the foldable plates of the micro-triangles.

The supporting frame (group #(1) in Fig. 4.3) was realized through 3D printed elements and fastened to a timber backing structure by means of twelve 6-mm stainless-steel screws.

Group #(2) comprises 3D printed slider blocks coupled to four metallic linear guides (7 mm thickness) supplied by Ftvogue and purchased via Amazon; the guides are connected by dedicated 3D printed junction pieces.

The group #(3) subassembly is made of four sets of 3D printed winch pulleys, each able to translate along 6-mm-diameter, flat-edged metallic guide rods obtained from a local supplier; these winches actuate the cable system responsible for the secondary motion.

Group #(4) contains 9-mm stainless-steel pulleys provided by Walfront (via Amazon) and nylon cables sourced locally. The selected PV panels are rectangular (25 mm $\times$ 30 mm), with nominal voltage 1 V and nominal current 80 MA. The foldable plates are attached to the supporting frames using 2.5-mm stainless-steel screws. The opening and closing cables associated with the primary folding motion have diameter 0.40 mm, whereas the bus cable has diameter 0.60 mm (see Fig. 4.3).

With reference to group #(5) in Fig. 4.4, the mock-up employs 3D printed covers to protect the pulleys. Such covers were mounted, by means of 2.5-mm stainless-steel screws, on the pulleys installed in the slider blocks, on the corner components of the frame, and at the module center.

Group #(6) consists of eight 3D printed micro-triangle frames, featuring PLA bars with 3 mm $\times$ 5 mm rectangular cross-section. For the experimental campaign, the structural set of a single micro-triangle (supporting frame, closure plate, and scissor pins) was additionally fabricated externally by Shapeways® (`https://www.shapeways.com/`) in Matte Black Steel.

Group #(7) collects the 3D printed tensegrity scissor mechanisms and the actuation cables used for the secondary folding motion. The latter are nylon lines with 0.4 mm diameter, identical to those adopted for the primary actuation, and they pass through ring pins positioned on the micro-triangle frames. The scissor bars have 2.8 mm $\times$ 1.5 mm rectangular cross-section and length 60 mm.

Finally, group #(8) comprises eight 3D printed foldable plates (3 mm thickness), each integrating six micro-PV panels purchased through AliExpress® (`https://www.aliexpress.com/`).

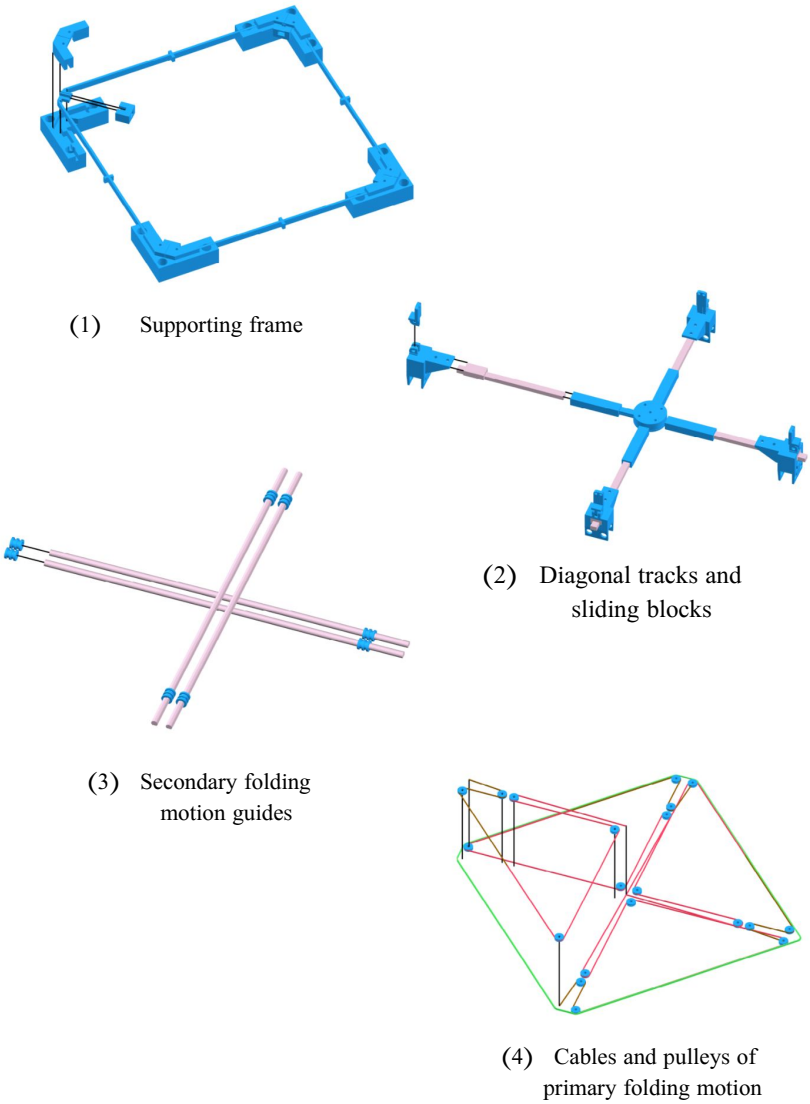

Figure 4.3: Exploded view of the groups (1)-(4) of components of the quadrangular module (reproduced from Fraternali et al., 2024b under the license CC BY-NC-ND 4.0).

(5) Pulley covers

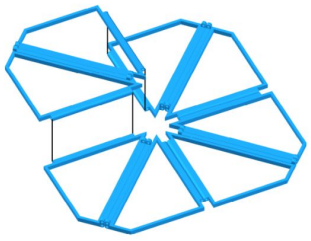

(6) Micro-triangle frames

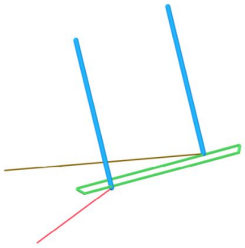

(7) Scissor structure and activation cables of secondary folding motion (8x)

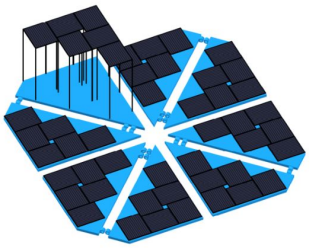

(8) Micro-triangle plates and PV/T panels

Figure 4.4: Exploded view of the groups (5)-(8) of components of the quadrangular module (reproduced from Fraternali et al., 2024b under the license CC BY-NC-ND 4.0).

4.2 Assembly method of the solid parts

This section describes the assembly procedure adopted for the rigid components of the prototype. Figure 4.5 illustrates the sequence of operations for the solid parts (i.e., excluding cables) located along one of the four diagonals of the module (Fraternali et al., 2024b). Since the four diagonals share the same layout, the procedure reported in the figure can be replicated without modifications for the remaining diagonal subassemblies.

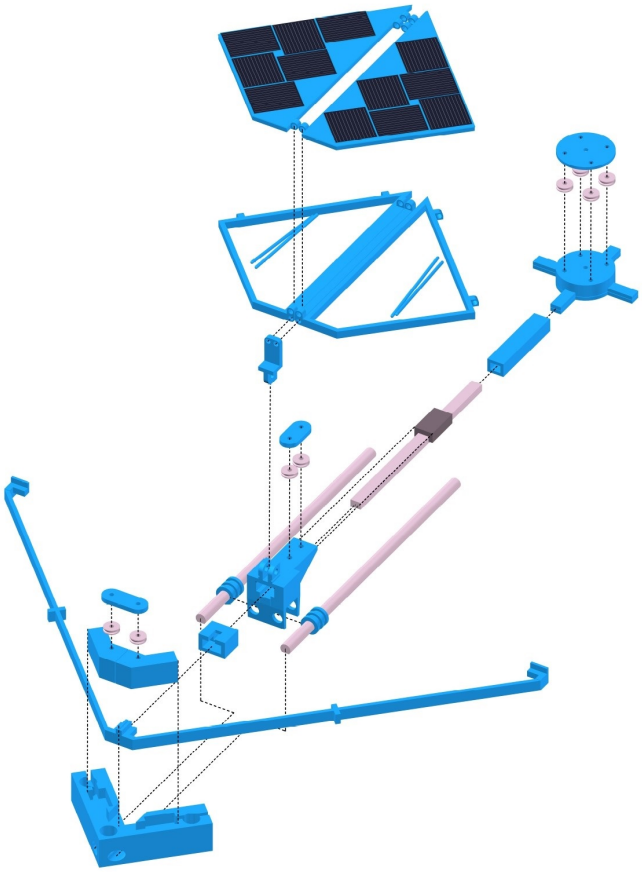

Figure 4.5: Assembly of the solid parts forming the center and one diagonal of the model (reproduced from (Fraternali et al., 2024b) under the license CC BY-NC-ND 4.0).

Within the demonstrator, short strips of paper tape were wrapped to obtain cylindrical hinges linking pairs of neighboring frames, as depicted in Fig. 4.6a and Fig. 4.6b. The adopted solution was inspired by tape-spring hinge concepts reported in Seffen and Pellegrino (1997) for deployable structural systems.

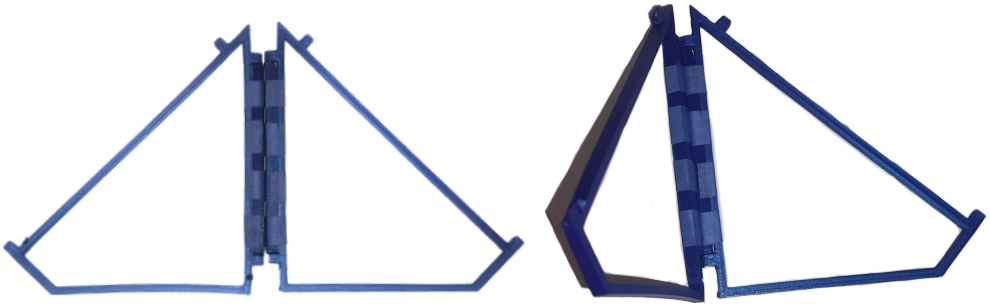

(a) Non folded micro-triangles **(b)** Partially folded micro-triangles

Figure 4.6: Paper tape hinges used for the connection adjacent micro-triangle frames (reproduced from Fraternali et al., 2024b under the license CC BY-NC-ND 4.0).

4.3 Actuation and folding motions of the prototype

This section presents the technical details of the primary and secondary folding motions of the quadrangular module. First, the sequence associated with the primary motion is described, and then the actuation and synchronization of the secondary folding of the micro-triangles are discussed.

The primary folding sequence was simulated in Autodesk Inventor®, and representative frames are reported in Fig. 4.7. The fully closed state is intentionally not perfectly planar: a small residual fold angle is introduced for the macro-triangles to enhance stability and to ease initiation of the actuation.

Primary folding is driven by the bus cable (green), to which the opening (red) and closing (brown) lines are attached through joints. For each opening/closing line, one extremity is anchored to the frame and the opposite extremity is coupled to the bus cable (Figure 4.3). Such a layout effectively reduces the actuation force required to move the sliders. By rotating the bus cable clockwise, the opening line is tensioned while the closing line is relaxed, which pulls the sliders toward the module center and induces opening.

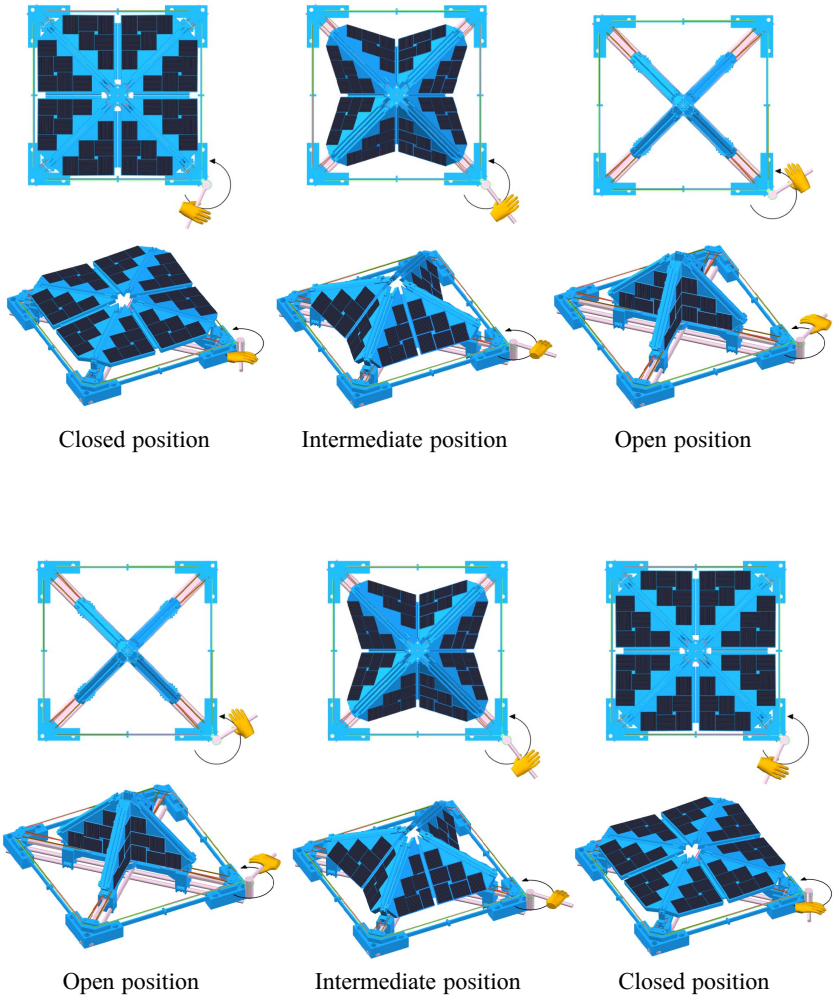

Figure 4.7: Opening and closing mechanisms of the primary folding motion of a quadrilateral module - Frontal and isometric views (reproduced from Fraternali et al., 2024b under the license CC BY-NC-ND 4.0).

In addition to this primary motion, the secondary folding motion of each micro-triangle is synchronized by the guiding bar shown in Fig. 4.8 (see also Fig. 4.3). Four guiding bars are employed overall: each is coupled to a winch/motor and commands the folding of two adjacent micro-triangles.

The opening and closing cables of the scissor mechanism (see Fig. 2.3) are routed over pulleys mounted on the corresponding guiding bar, as also illustrated by the Autodesk Inventor® snapshots in Fig. 4.8.

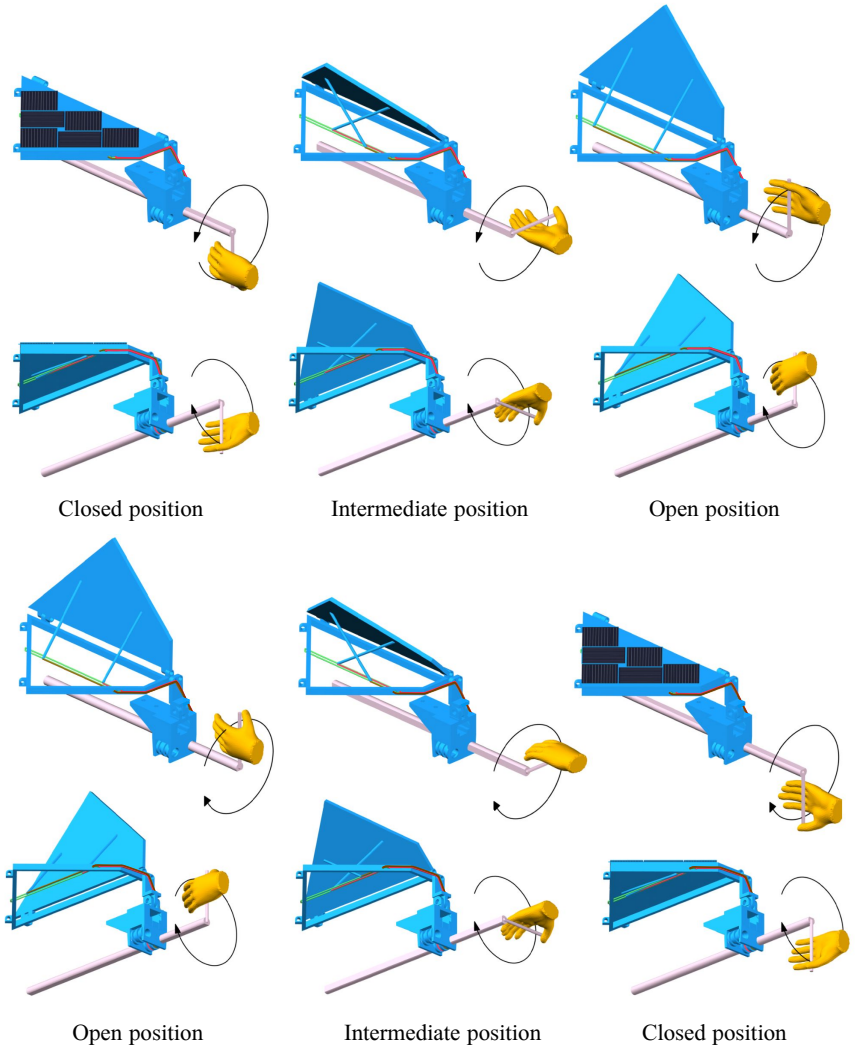

Figure 4.8: Different views of the opening-closing mechanism of a micro-triangle associated with the secondary folding motion (reproduced from Fraternali et al., 2024b under the license CC BY-NC-ND 4.0).

Building upon this routing scheme, the two folding modes are decoupled by positioning the pulleys that route the secondary actuation lines beneath the slider blocks associated with the primary motion (Fig. 4.9). These pulleys are free to translate along the longitudinal direction of the secondary guiding bars.

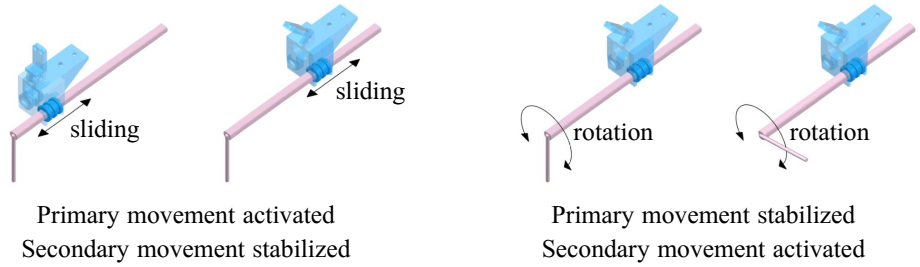

Figure 4.9: Movements of the pulleys guiding the secondary folding motion (reproduced from Fraternali et al., 2024b under the license CC BY-NC-ND 4.0).

Relative twisting between pulleys and guiding bars is prevented through flat edges machined/printed on both components (Fig. 4.10). Consequently, during actuation of the primary folding, the secondary system can remain stationary; conversely, when the secondary guiding bars are rotated about their axes, the attached pulleys rotate together and the secondary folding of the micro-triangles is triggered without affecting the primary motion.

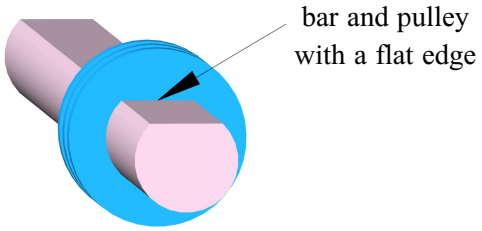

Figure 4.10: Presence of flat edges in the guides and pulleys of the secondary folding motion (reproduced from (Fraternali et al., 2024b) under the license CC BY-NC-ND 4.0).

The operation of the mock-up under these actuation schemes is illustrated in Figs. 4.11 and 4.12.

Fig. 4.11 reports representative frames extracted from videos documenting the primary folding of the mock-up; the module is shown in the fully open state, an intermediate state, and the open state.

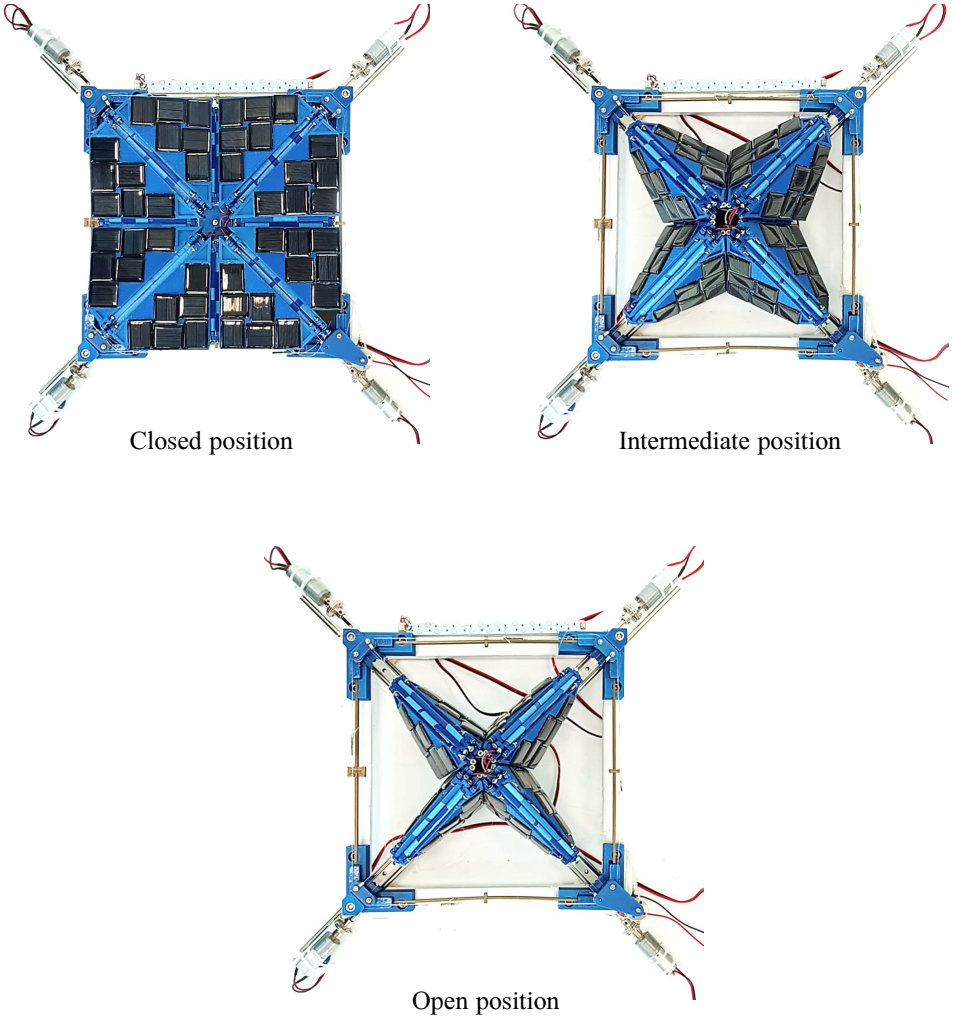

Figure 4.11: Frames extracted from a video of the opening and closing mechanisms of the primary folding motion of a 3D printed mock-up (quadrangular module) (reproduced from Fraternali et al., 2024b under the license CC BY-NC-ND 4.0).

Likewise, Fig. 4.12 shows frames extracted from videos of the secondary folding motion. Starting from the open state of the primary motion, the sequence displays a representative micro-triangle in the closed, intermediate, and fully open secondary configurations.

Closed position

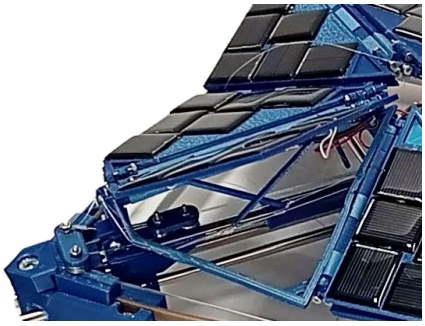

Intermediate position

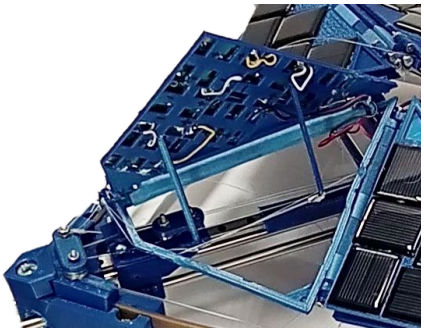

Open position

Figure 4.12: Frames extracted from a video of the opening and closing mechanism of the secondary folding motion of a 3D printed mock-up (quadrangular module) (reproduced from Fraternali et al., 2024b under the license CC BY-NC-ND 4.0).

4.4 Electronic actuation and control of the module

Building on the mechanically actuated folding mechanisms described in the previous section, this section details the electronic actuation and control architecture implemented in the quadrilateral demonstrator. The prototype integrates five DC motors supplied by Dewin (via Amazon), rated at 12 V with a nominal speed of 15 revolutions per minute (RPM) (Fig. 4.2).

A single motor, mounted with vertical axis in the bottom-right corner of the prototype (Fig. 4.2), drives the primary folding motion. This motor is coupled to the perimeter bus cable through a 3D printed pulley and a 4-mm metallic flange connector supplied by Winwill (via Amazon).

The remaining four motors are installed with horizontal axes at the four corners of the device and command the secondary folding, each motor actuating two micro-triangles (Fig. 4.2). These motors are linked to the guiding bars through 6-mm metallic flange connectors. The actuation hardware includes three L298N motor-driver boards, each capable of controlling two motors. One driver is dedicated to the primary motion, while the other two drivers operate the sets of guiding-bar motors associated with the secondary motion. Motor commands are generated by an Arduino board interfaced with a personal computer through serial communication.

The realization of the quadrilateral TensOri demonstrator provides a complete experimental platform for testing the kinematic and mechanical principles introduced earlier. The component architecture and the described assembly steps permit independent actuation of the primary and secondary folding motions, and the motorized layout confirms the practicality of cable-driven control with low-power actuators. The prototype also establishes a baseline for subsequent iterations and for scaling toward larger systems. The next chapter addresses the tessellation of multiple solar eyes into a photovoltaic window and discusses the related implications for adaptive building façades.

5

Implementation of Solar Eye Modules in an Origami PV Window

This chapter investigates how the quadrilateral solar-eye modules introduced in the previous chapters can be assembled into a tessellated configuration to form a prismatic photovoltaic window, hereafter referred to as the 'TensOri' window, conceived for integration within an adaptive building envelope. It expands and further develops results originally presented in the following bibliographic paper, coauthored by the PhD candidate and cited in the bibliography as Fraternali et al. (2024a):

Fraternali, F., Babilio, E., Nazifi Charandabi, R., **Germano, G.**, Luciano, R., Spagnuolo, G. (2024) *Dynamic origami solar eyes with tensegrity architecture for energy harvesting Mashrabiyas*. Applications in Engineering Science 19,100190,2024.

5.1 TensOri window mock-up

This section describes the construction of a TensOri window comprising multiple Solar Eye modules. To maximize energy harvesting, the panels within each module should be oriented toward the sun. Since the modules are distributed in a matrix layout, a dedicated mechanism was devised to coordinate the primary and secondary motions across the array while minimizing the number of actuators. Fig. 5.1 shows a prototype window assembled from 13 Solar Eye modules in the closed configuration, while Fig. 5.2 illustrates the corresponding open configuration. Along the perimeter, fixed infill panels were added to close the gaps between the tessellated modules and the external frame.

The tessellated layout was obtained by removing the individual module frames and coupling neighboring modules along the linear bearing guides, thereby creating a continuous cross-sectional assembly. All profiles are then fastened to a new supporting frame designed to be mounted to the veranda structure. The primary folding motion, which translates the linear bearings along their guides to open and close the Solar Eye modules, is coupled to a single activation line (termed the secondary bus cable). This line is, in turn, connected to a cable running along the external frame (termed the primary bus cable). A close-up of the joints is shown in Fig. 5.4 and is discussed in Sect. 5.2.

The secondary motion, responsible for unfolding the individual panels, is produced by rotating the guiding bars located beneath the profiles; through winches and cables, such rotation is transmitted to the panels. This architecture allows one guiding bar to serve multiple adjacent modules. Moreover,

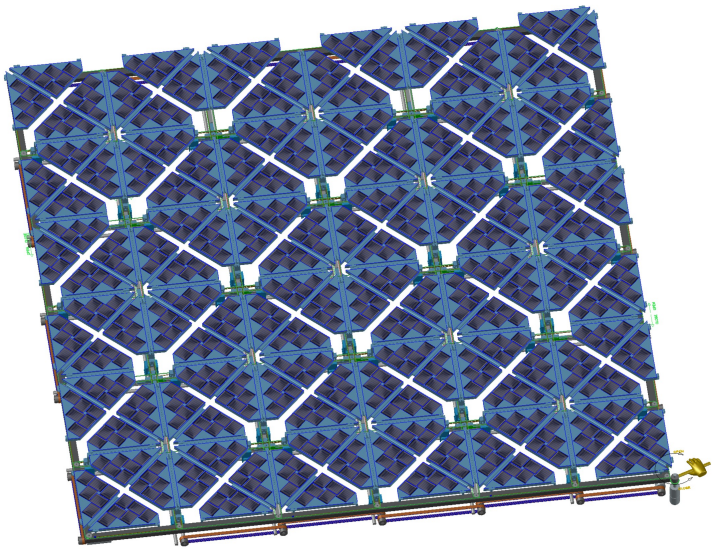

Figure 5.1: View of the TensOri window with closed panels.

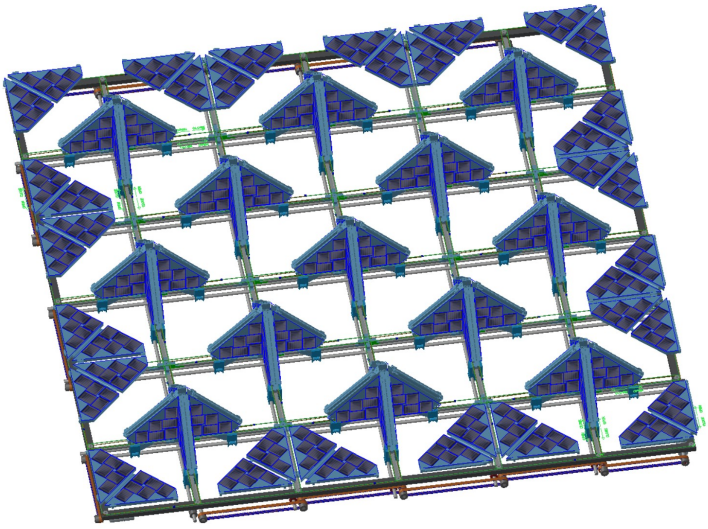

Figure 5.2: View of the TensOri window with open panels.

the guiding bars associated with each set of parallel modules are mechanically linked by toothed belts, so that a single actuator can drive the corresponding panel motion across the array.

As a result, operation of the TensOri window requires one gearmotor for the primary motion (opening/closing of the Solar Eye modules) and four gearmotors to actuate the microtriangle pairs responsible for solar tracking. Assuming installation on a south-facing façade, the two microtriangles on the right side of the Solar Eye vertical axis can be rotated to approximately 90 degrees at sunrise and then progressively lowered to follow the sun until noon. After noon, the microtriangles on the left side can be gradually raised from their resting configuration, reaching approximately 90 degrees by sunset as the sun moves toward the west.

In an analogous manner, the two microtriangles located below the horizontal axis of the Solar Eye can be tilted as a function of the solar azimuth throughout the day.

After sunset, the microtriangles may be returned to the neutral configuration (zero tilt), while the window can be opened or closed via the primary motion to regulate daylight and ventilation within the veranda.

For a vertical window installation, the actuation of the two microtriangles above the horizontal axis is not required; however, this additional degree of freedom becomes relevant for a horizontally oriented window placed above the veranda.

5.2 TensOri window Kinematics

In this section we describe the kinematics of the TensOri window.

For the underlying module mechanism, the reader is referred to Sect. 2.2, where the kinematics of the Solar Eye module are introduced. Figure 5.3 shows the window in the open configuration without the upper panels, so that the kinematic layout is visible. The figure highlights the sliders in their fully open position, the cable–pulley network governing the primary motion (with the motor located at the bottom-right corner), and the guiding-bar and toothed-belt system along the four sides that controls the secondary motion, together with the corresponding motors.

The coordinated operation of the two motions is discussed below. Figure 5.4 shows a cross-sectional view of the primary-motion transmission.

For clarity, the linear-guide support profiles and the external frame are

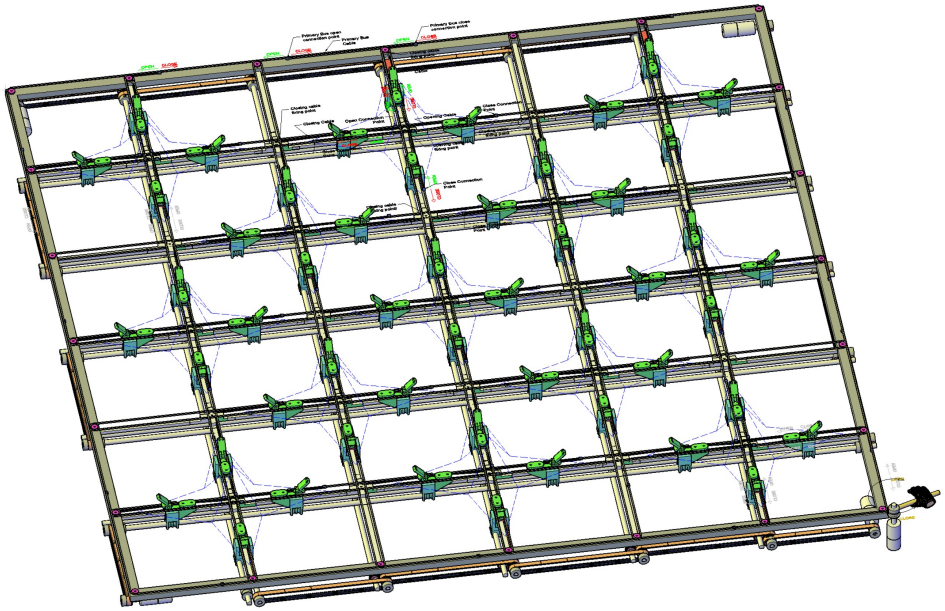

Figure 5.3: View of the TensOri window in the opened position without panels.

omitted from the figure. The primary bus cable (gray) runs along the upper portion of the external frame, and the secondary bus cables are connected to it by splices. A dedicated splice detail connects the primary bus cable, the secondary buses, and the opening/closing lines, ensuring that clockwise rotation of each loop produces closure.

The splices are positioned so that they do not interfere with pulley passages, thereby preventing jamming. The splice on the primary bus cable connects:

- the opening line of the secondary bus associated with the module column to the right of the joint;
- the closing line of the secondary bus associated with the module column to the left of the joint;
- the closing line of the upper module to the left of the joint.

By symmetry, an analogous arrangement applies to the secondary bus cables in the horizontal direction. During an opening maneuver (green-arrow direction

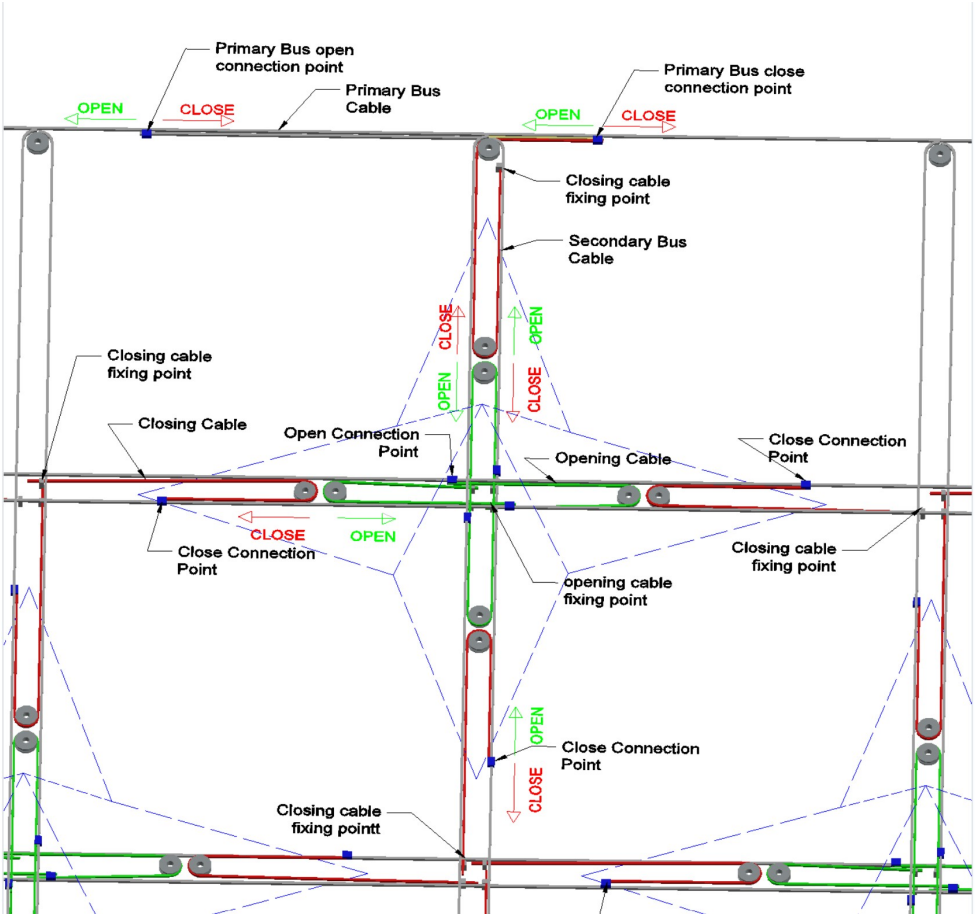

Figure 5.4: Opening-closing mechanism of the primary folding motion of a TensOri window obtained by changing the rest length of the activation cables.

in Fig. 5.4), the loops rotate counterclockwise: the closing lines (red) are slackened while the opening lines (green) are tensioned, so that all Solar Eye modules open simultaneously.

As in the single-module configuration, each opening/closing line of the primary motion is anchored to the structure at one end and connected to the bus cable at the other. This routing yields a mechanical advantage at the slider, effectively doubling the slider force relative to the line tension, which is beneficial in the initial phase when the module starts from the fully deployed

configuration.

The secondary motion is transmitted to each microtriangle through the lower guiding bars, as illustrated for the single module in Fig. 4.8 (Chapter 4). Owing to the guiding-bar profile, the winches can translate during the primary motion without coupling into the secondary actuation. Figure 5.5 summarizes the kinematic layout for the secondary motion.

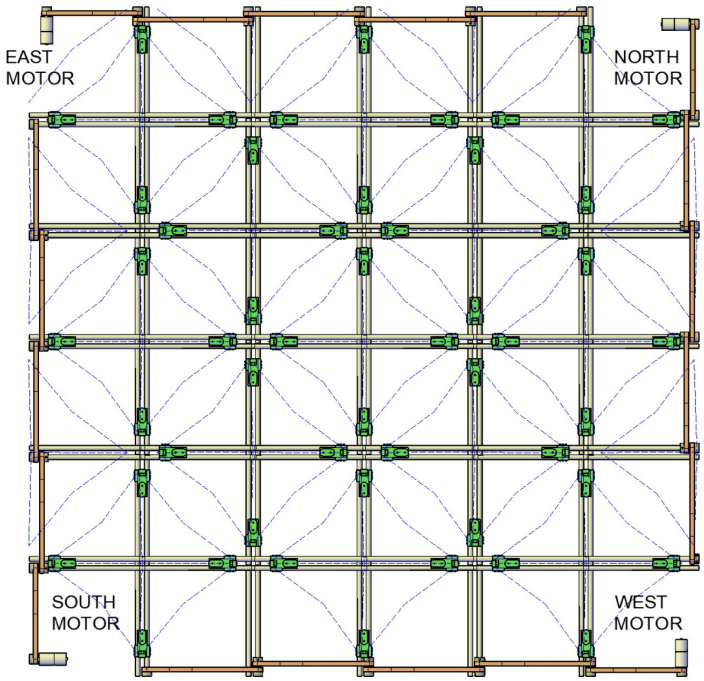

Figure 5.5: Opening-closing mechanism of the secondary folding motion of a TensOri window obtained by guiding bars rotation.

To improve readability, the figure omits the panels, the external frame, and the primary-motion cable system. In Fig. 5.5, a motor is placed at each edge of the window, and toothed belts along the perimeter couple the homologous guiding bars associated with the microtriangle pairs above the horizontal axis.

The motor located at the top-left corner (labeled 'East Motor') is connected, through toothed belts and pulleys, to the guiding bars on the left side of the vertical axis. Via winches positioned beneath the green sliders, these guiding bars actuate the cables controlling the left panels (upper and lower),

enabling the corresponding microtriangles to rotate toward the east, thereby improving energy capture from dawn to midday.

The motor at the top-right corner (labeled 'North Motor') drives the guiding bars located above the horizontal axis. These bars are connected to the cables controlling the two upper panels (left and right), enabling downward rotation of the upper microtriangles. While this motion is not primarily intended to increase energy production in the vertical-window configuration, it can be exploited to enhance daylight admission into the veranda.

The motor at the bottom-right corner (labeled 'West Motor') drives the guiding bars to the right of the vertical axis. The attached cables actuate the right panels (upper and lower), allowing the corresponding microtriangles to rotate toward the west, which is beneficial for energy capture after noon.

Finally, the motor at the bottom-left corner (labeled 'South Motor') drives the guiding bars below the horizontal axis. These bars actuate the cables controlling the two lower panels (left and right), enabling upward rotation of the lower microtriangles, which supports sun tracking by adjusting the tilt according to the solar azimuth during the day.

6

Mechanical Design and Manufacturing of a Prototype of a Smart PV Window

This chapter was developed in strict collaboration with the research group led by César Domínguez at the Instituto de Energía Solar (IES), Universidad Politécnica de Madrid (UPM), and in close cooperation with Rana Nazifi Charandabi, a PhD student in Photovoltaics at the University of Salerno, during her research internship at UPM. It focuses on the design and fabrication of a controlled actuation mechanism for a smart window (hereafter referred to as SMARTWIN) integrating concentrator photovoltaic technologies. The architectural and photovoltaic design of SMARTWIN was developed by the aforementioned research group at IES and is presented in Garcia-Sanchez et al. (2025).

6.1 The SMARTWIN system

In Garcia-Sanchez et al. (2025), the UPM research group has presented an innovative semi-transparent double-glazed BIPV system that employs concentrator photovoltaics combined with an integrated tracking mechanism. By directing direct sunlight onto the embedded solar cells, the system efficiently generates electricity while permitting diffuse light to pass through, ensuring pleasant natural illumination and reducing glare without relying on blinds. This functionality is realized through a solar concentration system composed of horizontal lenses that focus the sun's rays onto photovoltaic stripes.

Since the sun's rays reach the lenses at varying angles throughout the day and across seasons, the focal point projected behind each lens also shifts in both height and depth. To address this challenge, the objective of this chapter is to design an actuation mechanism for the SMARTWIN system that enables the internal window panel to move accordingly, maintaining precise solar concentration under changing conditions.

As illustrated in Figure 6.1, the lens mounted on the exterior pane of a south-facing window converges incoming solar radiation onto a focal point located behind the lens. Following the apparent path of the sun, this focal point travels along an arc, exhibiting dynamic variations in its horizontal offset from the glass and vertical displacement relative to the lens's optical axis.

To optimize energy capture, a secondary glass panel positioned at the rear contains photovoltaic (PV) strips aligned parallel to the lenses. This panel integrates a dual-axis tracking system—both horizontal and vertical—that continuously adjusts the position of the PV strips to coincide with the moving focal point of the concentrated rays. In doing so, this chapter bridges the

gap between static window-integrated PV systems and adaptive concentrating technologies capable of maintaining optimal alignment for maximum efficiency.

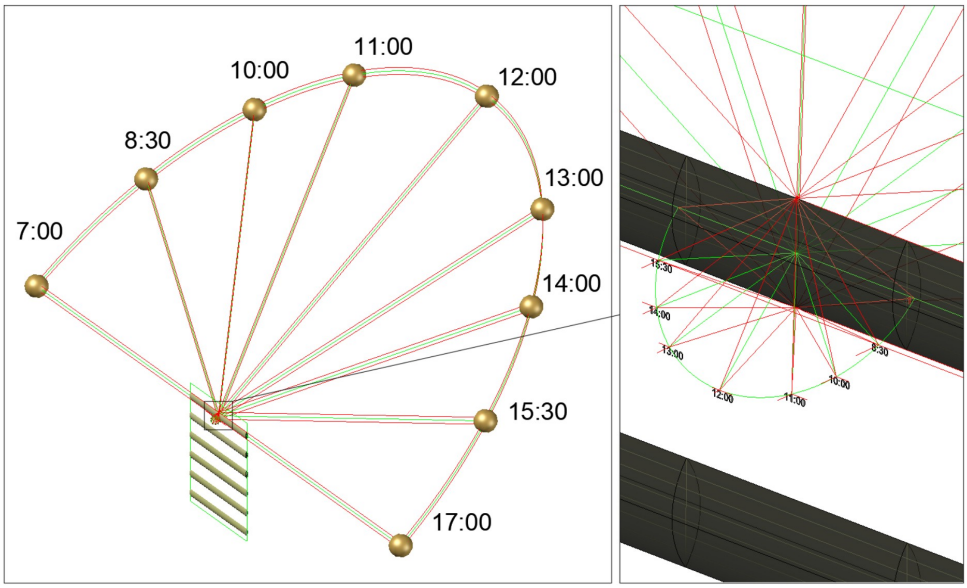

Figure 6.1: Concentration of solar rays using a Fresnel lens.

6.2 Design and Kinematics of a SMARTWIN prototype

This section presents the design and kinematics solution adopted for the SMARTWIN prototype, describing the overall structural layout of the frame and the moving internal panel, as well as the actuation strategy for vertical and horizontal tracking. The prototype was developed using 3D CAD modeling and is based on an aluminum frame that supports the external glazing with linear concentrating lenses and an internal panel carrying the photovoltaic strips. The PV strips are arranged with the same pitch as the lenses (22.5 cm), and the main external and internal dimensions of the window are summarized in the CAD layout shown in Fig. 6.2.

Based on the specifications of the photovoltaic strips—consisting of 8 mm wide bare cells with a length of 300 mm—the dimensions of the internal panel

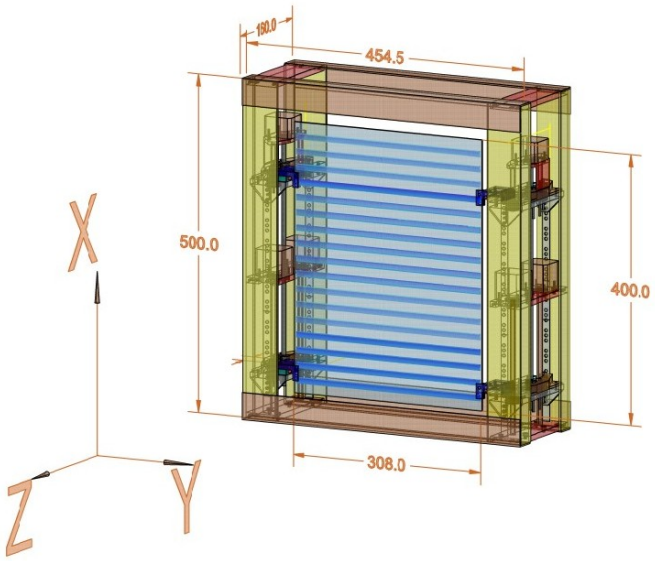

Figure 6.2: 3D CAD model of SMARTWIN.

were defined as follows. The width (Y-direction) was set to 308 mm, accounting for the 300 mm cell length plus the clearance required to securely fasten the panel to its mechanical supports. The height (x-direction) was fixed at 400 mm, corresponding to the integration of 17 photovoltaic strips. This layout results from the 22.5 mm pitch (center-to-center distance) of the linear Fresnel lenses, ensuring that each strip is aligned with its corresponding lens for maximum optical concentration.

The frame dimensional design was then completed by considering the physical dimensions of the motors and vertical linear bearings, as well as the vertical and horizontal travel ranges that will be further defined in Section 6.2.1. This resulted in a depth of 160 mm (Z-direction). Using the selected aluminum profile cross-sections within the CAD environment, the overall structural envelope was determined, as illustrated in Fig. 6.2

The remaining mechanical components were conceived to be manufactured in ABS using 3D printing, a choice that guided the design of the connection details and support elements and will be revisited in the fabrication section, where the realization of the prototype is discussed.

6.2.1 Vertical and Horizontal Movements

The SMARTWIN system is designed to provide controlled bi-axial movement of the internal panel so that the photovoltaic (PV) strips can follow the focal line of the concentrating lenses throughout the day and across seasons. Moving the internal panel vertically requires overcoming the combined weight of the polycarbonate plate, the PV strips, and the associated mechanical components. In contrast, horizontal movement demands significantly less force, as the use of linear bearings substantially reduces friction. For this reason, four motors were adopted to drive the vertical motion, while two motors are sufficient for the horizontal displacement.

The vertical motors are mounted on the frame, whereas the horizontal motors are installed on the upper mechanism to drive both the upper and lower parts of the system. The control strategy synchronizes the motors so that the panel moves smoothly and precisely along both axes.

Figure 6.3 shows one of the two lateral sections of the mechanism. The vertical motion sequence starts with the simultaneous activation of the two vertical motors (1), which are fixed to the frame via motor supports. These motors drive the ball screws (4), causing the lower horizontal mechanism (8) to translate. This motion is transmitted to the linear guide (9) and the upper mechanism (7), so that the polycarbonate panel, attached to the linear bearing (6), rises uniformly on both sides of the window.

Once the desired vertical position is reached, the horizontal motion is activated. The horizontal motor (2) turns the central shaft, which drives the pulley connected to the toothed belt. The rotation of the pulley moves both the upper and lower runs of the belt, and this displacement is transferred to the linear bearing (6). As a result, the bearing slides along the linear guide, shifting the polycarbonate panel in the horizontal direction, as illustrated in Fig. 6.4.

The admissible ranges for vertical and horizontal displacement were defined from the optical analysis of the SMARTWIN concept carried out by the UPM research group, which determined the motion required to keep the PV strips close to the focal line over the relevant solar positions (Garcia-Sanchez et al., 2025). In the final design, the internal panel can move from 0 to 51 mm along the vertical x-axis (total travel 51 mm) and from -75 to -7 mm along the horizontal Z-axis (total travel 68 mm). These constraints provided the baseline for sizing the SMARTWIN window assembly and for selecting the actuation components.

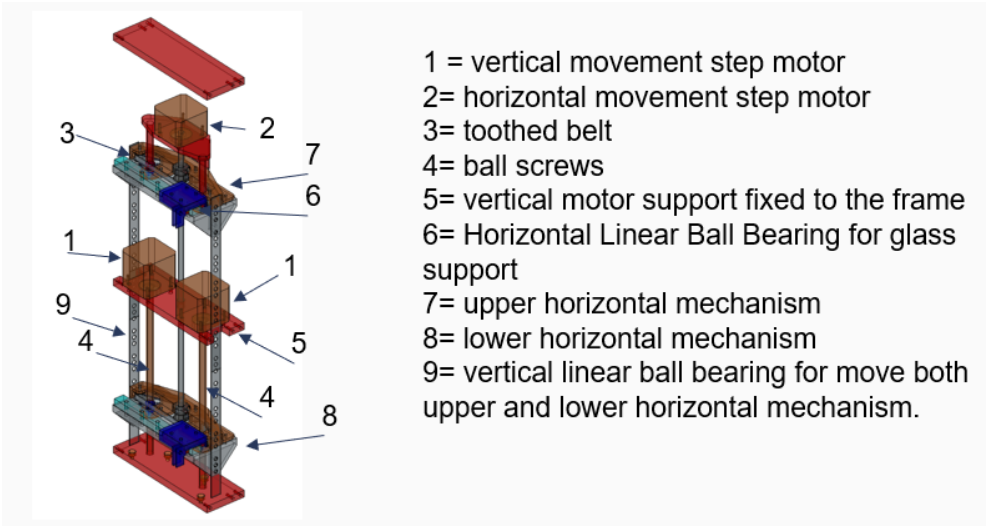

Figure 6.3: Left section of the SMARTWIN prototype.

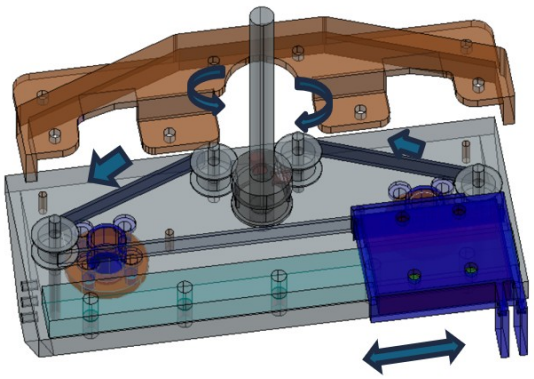

Figure 6.4: horizontal mechanism

6.2.2 Actuation strategy and positioning resolution

The SMARTWIN panel is actuated along two independent axes: a vertical axis to compensate for the height variation of the focal line and a horizontal axis to follow its depth variation within the glazing cavity. Vertical displacement is generated by a pair of stepper motors driving ball screws, while horizontal positioning is obtained through a dedicated stepper motor and a belt–pulley transmission. This dual-axis actuation strategy enables precise alignment of the internal panel with the solar focal line within the available space between the external and internal glazing.

From a functional standpoint, the glass assembly must achieve accurate biaxial movement inside the frame, while avoiding collisions with the fixed outer pane and preserving sufficient clearance for installation and operation. High-precision positioning is essential to maintain the concentrated solar radiation on the photovoltaic strips and thus maximize the electrical energy yield.

For the vertical movement, the mechanism is designed to support the combined weight of the polycarbonate plate, the PV strips, and the attached hardware. The two vertical stepper motors are fixed to the frame and drive the ball screws; these in turn translate the lower horizontal assembly along a linear guide. Since the upper assembly is linked to the same guide, both move synchronously, lifting or lowering the internal panel as a rigid body.

The horizontal movement only requires sliding the panel along the guide, so a belt–pulley system is adopted for simplicity and efficiency. The horizontal motor drives a 20-tooth central pulley, which moves the toothed belt connected to the horizontal bearing attached to the polycarbonate panel, thereby producing the required in-plane displacement.

The actuation system uses stepper motors with a basic resolution of 1.8° (200 steps per revolution), combined with microstepping drivers (e.g. A4988) to increase positioning granularity. In the vertical axis, with a screw pitch of 2 mm, the resulting displacement per full step is

$$\text{Resolution}_v = \frac{2 \text{ mm}}{200 \text{ steps}} = 0.01 \text{ mm/step}.$$

For the horizontal axis, the toothed belt is driven by a 20-tooth pulley corresponding to 20 mm of linear travel per revolution; using 800 microsteps per revolution in quarter-step mode yields

$$\text{Resolution}_h = \frac{20 \text{ mm}}{800 \text{ microsteps}} = 0.025 \text{ mm/microstep}.$$

These resolutions are sufficient to finely position the panel within the admissible ranges defined in the previous subsection.

6.3 Manufacturing of the SMARTWIN Prototype

Following the design outlined in Section 6.2, a full-scale prototype of the SMARTWIN system was manufactured to validate the proposed actuation concept under realistic conditions. The mechanical architecture is based on an aluminum frame supporting the external glazing with linear Fresnel lenses and an internal movable panel in polycarbonate, conceived to host the photovoltaic strips with the pitch imposed by the optical design. The prototype dimensions and material choices were directly derived from the CAD model presented in Fig. 6.2, ensuring consistency between the simulated kinematics and the physical realization.

Figure 6.5 shows a front view of the assembled mock-up; in this configuration, the external glazing containing the linear Fresnel lenses has been removed, and the internal panel appears as a transparent polycarbonate sheet prior to the application of the solar strips.

6.3.1 Actuator implementation and kinematic supports

Figure 6.6 shows the right-hand side of the mechanism, where the two vertical motors, labeled MXRI and MXRE, are installed. The naming convention adopted for the actuators is as follows: Motor, x-axis, Right side, Interior (MXRI) and Motor, x-axis, Right side, Exterior (MXRE), where the x-axis denotes the vertical movement of the system. The components highlighted in grey are 3D-printed in ABS, reflecting the design choice discussed in Section 6.3.

Several key technical solutions for the kinematic support and load transfer can be observed in this view. At the bottom, two bearings support the threaded rods, allowing smooth rotation while transmitting the combined weight of the internal panel and the horizontal mechanism directly to the base of the frame. The vertical motors are secured to the frame by 3D-printed lateral brackets and coupled to the threaded rods through flexible couplings, which are essential to accommodate possible axial and radial misalignments. Vertical actuation is achieved via lead nuts integrated into the ABS support structure of the horizontal mechanism, which is lifted as the rods rotate. The

Figure 6.5: Front view of the SMARTWIN mock-up.

figure also shows the drive shaft connected to the horizontal actuator (not visible in this view) and the linear guide support for the polycarbonate panel, which is likewise manufactured in ABS. A green LED indicates the status of the limit switch (end-stop) used to ensure accurate zero-positioning (homing) of the Z-axis.

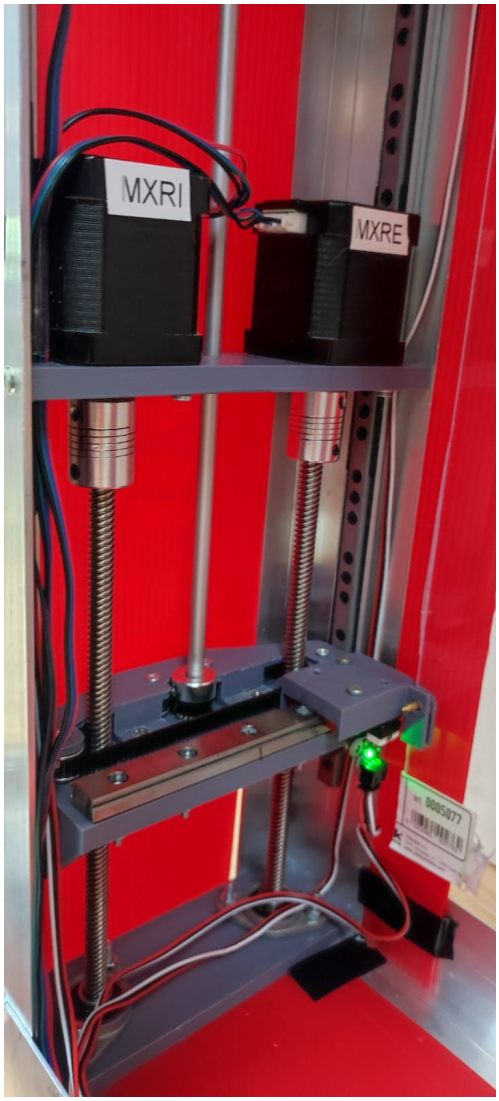

Figure 6.6: Right side of the mechanism with the vertical motors.

Figure 6.7 illustrates the top-right section of the mechanism, where the horizontal motor labeled MZR (Motor, Z-axis, Right side) is located. This actuator is mounted on a 3D-printed ABS support that is fixed to the upper horizontal assembly and therefore moves synchronously with it. The motor shaft is connected to the transmission rod via a flexible coupling, again to compensate for potential misalignments. The same figure highlights the attachment of the horizontal movement support to the lateral metal guide. This guide, which has three mounting holes, slides within a track fixed to the frame and is mechanically linked to the lower horizontal assembly, ensuring synchronized horizontal motion across the system.

In Figure 6.8, a yellow circle marks the two vertical limit switches (end-stops) responsible for the accurate zero-positioning (homing) of the x-axis. Each switch is associated with one of the vertical motors. During the initial homing sequence, the horizontal mechanism assembly moves upward until both switches are activated; this dual-sensor configuration is critical to guarantee the correct alignment and horizontality of the entire moving assembly.

6.3.2 Microprocessor control system

The control architecture manages a total of six stepper motors and six limit switches (end-stops). The motors are driven by six A4988 (Allegro MicroSystems, 2022) stepper drivers, arranged on two CNC shields, one for each side of the SMARTWIN window. This configuration provides a compact and modular interface for multi-axis motion control using standard step and direction signals (Gandolfo, 2023).

All motors are supplied from a 12 V DC source, which can be provided by a rechargeable battery integrated into the window's energy-harvesting system. The central control unit is an ESP32 microcontroller, a low-cost, low-power system-on-chip (SoC) featuring a dual-core processor and integrated Wi-Fi and Bluetooth connectivity (Espressif Systems, 2025). These communication capabilities enable both local wireless access and potential integration into building automation networks.

Figure 6.9 illustrates the control hardware assembly. To the left of the ESP32, a Real-Time Clock (RTC) module is installed to maintain accurate timekeeping during power interruptions via a dedicated backup battery. On the right, two CNC shields are mounted, each populated with three A4988 drivers for stepper motor actuation.

The microcontroller is configured to connect to a Wi-Fi network using a

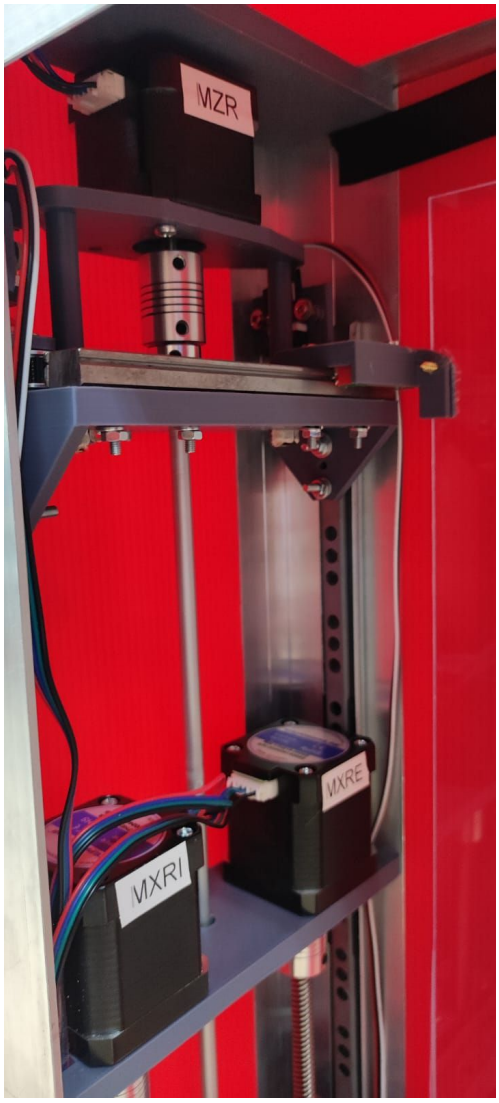

Figure 6.7: Top-right section of the mechanism with the horizontal motor.

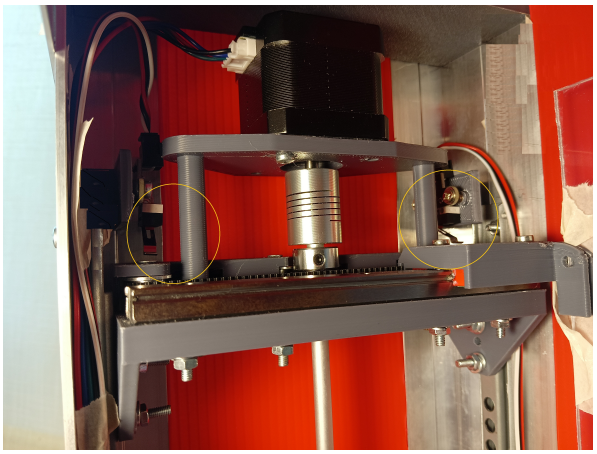

Figure 6.8: Upper limit switches for vertical movement.

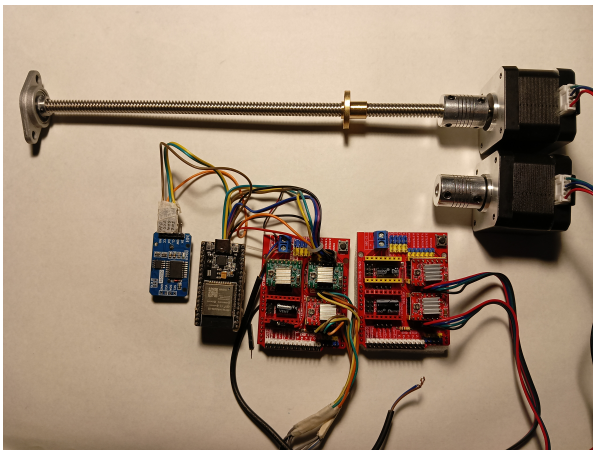

Figure 6.9: Control electronics of the SMARTWIN prototype.

predefined SSID and password. It hosts an internal web server that provides a graphical interface for manually setting the X and Z coordinates, corresponding to the vertical and horizontal positions of the internal panel; this functionality is particularly useful for laboratory tests on energy harvesting and daylighting performance.

In autonomous mode, the ESP32 uses a solar position library (Willmott, 2019) to compute the current solar elevation and azimuth from the site's geographic coordinates and the time information supplied by the RTC. By means of look-up tables and calibration data obtained from the optical analysis performed by the UPM group, the controller converts the sun position into target X and Z values for the stepper motors. Under standard operation, the control algorithm maximizes the irradiance on the PV strips; however, a configurable offset can be applied to shift the focal line partially or completely between the strips, thereby increasing the transmitted daylight when required.

6.3.3 Concluding remarks

The present chapter has outlined the design, fabrication, and principal operating modes of the SMARTWIN prototype, with particular emphasis on construction details, kinematic mechanisms, and the actuation and control architecture. The solutions adopted demonstrate the feasibility of integrating solar shading and energy generation within a single system, while preserving a relatively simple mechanical configuration suitable for full-scale experimentation. The results obtained from the SMARTWIN mock-up thus provide a robust operational basis for future investigations aimed at further assessing the system's performance and exploring its potential applications in the building sector.

7

Concluding remarks and future perspectives

This thesis has presented the design, modeling, and experimental prototyping of a new class of adaptive structural modules based on tensegrity principles. The proposed systems are conceived as lightweight, deployable, and reconfigurable structures whose geometry and mechanical response can be actively governed through a limited set of actuation cables. By coupling adaptive, and in several instances origami-inspired, kinematics with tensegrity-based load transfer, the developed modules can tessellate planar or moderately curved surfaces in multiple layouts while preserving structural efficiency and maintaining modest actuation energy demands. Such a combination is particularly attractive for architectural-scale applications, where weight, ease of deployment, and controllable stiffness represent simultaneous and often competing requirements.

A central contribution of this work lies in the systematic investigation of the kinematic and mechanical behavior of the examined tensegrity–origami modules, with emphasis on how relatively simple cable operations can generate rich and controllable shape changes. Adjustable cable rest lengths enable deliberate morphing through primary and secondary folding motions, thereby supporting transitions among compact, deployed, and intermediate states. This actuation philosophy, together with the use of arbitrary polygonal geometries rather than a single canonical unit cell, distinguishes the proposed approach from earlier origami-based adaptive structures, which frequently rely on discrete hinges, concentrated rotational springs, or widespread actuation across many degrees of freedom. The results demonstrate that complex deployment paths and mechanical adaptability can be achieved through sparse control architectures centered on pretension management and cable length regulation, providing a practical route to scalability.

The mechanical performance of the modules has been analyzed through a combination of analytical formulations, numerical simulations, and experimental validation on reduced-scale prototypes. The modeling framework clarifies the roles of geometric nonlinearity, cable engagement and slackening, and prestress in shaping the force–displacement response. In particular, the post-deployment locking of selected cable rest lengths has been shown to stabilize the folding mechanisms and to provide a substantial increase in stiffness against external actions, including wind-induced effects. Modal analyses performed on representative quadrilateral configurations have further highlighted the dynamic characteristics of the system, revealing a separation between low-frequency modes associated with cable-governed motions and higher-frequency

modes dominated by the deformation of stiffer supporting elements. In parallel, simplified procedures to estimate the effects of wind loading have been outlined, suggesting that additional protection against extreme conditions may be provided through auxiliary restraining elements (e.g., motion stoppers) and/or dissipation devices. These additions are conceptually consistent with the present architecture and represent a direct and natural extension of the developed prototypes.

Beyond static and quasi-static considerations, the adaptive nature of the proposed tensegrity systems points to significant potential in applications requiring tunable dynamic response. Future investigations will therefore focus on characterizing structural behavior under seismic and other dynamic loading conditions by combining laboratory testing, advanced numerical modeling, and comparisons with recorded ground-motion inputs. In this context, the ability to modify stiffness, geometry, and load paths through controlled reconfiguration may enable new strategies for vibration mitigation, targeted energy dissipation, and adaptive seismic resilience. Such studies will necessarily incorporate large-displacement effects, nonlinear dynamics, and stability considerations, while also motivating the development of control algorithms capable of real-time adaptation under uncertain loading scenarios and practical actuation limits.

While the thesis primarily concentrates on structural mechanics and deployable behavior, selected application scenarios have been explored to demonstrate versatility and to clarify how functional components can be embedded within the structural concept. In particular, the integration of photovoltaic and solar-thermal elements within the rigid components of the modules has been investigated as a representative case study. A TensOri window system equipped with foldable energy-harvesting panels and sun-tracking capabilities has been proposed to illustrate how such structures may operate as adaptive building-envelope components. Moreover, a SMARTWIN smart PV window prototype has been designed and manufactured to demonstrate the implementation of vertical and horizontal positioning and an embedded control system at the scale of a full window module. Owing to low-energy actuation, modularity, and the possibility of distributed control, these systems appear promising for energy-efficient buildings, especially where adaptability, daylight modulation, and architectural integration are simultaneously required. At the same time, the energy-harvesting examples should be viewed primarily as demonstrators: the underlying structural principles are not tied to a specific function

and can be transferred to a much broader range of engineering contexts.

Future developments will expand the scope of the proposed systems toward broader structural and multidisciplinary applications. Candidate directions include deployable protective structures, adaptive shading and screening devices, reconfigurable load-bearing components, and smart structural subsystems for vibration and seismic control. From a systems perspective, further research is needed on the coordinated control of multi-module assemblies, including the definition of robust actuation layouts, fault-tolerant strategies, and optimization of cable routing and pretension levels. Additional studies will address manufacturability and durability at larger scales, long-term performance of cables and joints under cyclic operation, component reuse, life-cycle assessment, and the adoption of sustainable materials. Finally, the integration of alternative actuation technologies—such as shape-memory alloys, electroactive polymers, compact clutches, or other smart-material solutions—may further enhance responsiveness and resilience while reducing mechanical complexity in specific deployment scenarios.

Overall, this thesis demonstrates that tensegrity–origami systems constitute a promising structural paradigm for the development of adaptive, deployable, and mechanically efficient engineering solutions. By bridging geometry, mechanics, control, and prototyping, the work lays a foundation for future research on reconfigurable structures capable of responding intelligently to changing environmental and operational conditions across multiple areas of structural engineering and design.

Bibliography

Allegro MicroSystems (2022). *A4988: DMOS Microstepping Driver with Translator and Overcurrent Protection.* Accessed February 2026. Allegro MicroSystems, LLC. URL: https://www.allegromicro.com/-/media/files/datasheets/a4988-datasheet.pdf.

Armstrong, A., G. Buffoni, D. Eames, R. James, L. L. J. Lyle, and K. Xuereb (2013). "The Al Bahar towers: multidisciplinary design for middle east high-rise". *The Arup Journal* (2), 60–73.

Budiansky, B. (1974). "Theory of Buckling and Post-Buckling Behavior of Elastic Structures". *Advances in Applied Mechanics* 14 (C), 1–65. DOI: 10.1016/S0065-2156(08)70030-9.

Chen, T., O. R. Bilal, R. Lang, C. Daraio, and K. Shea (2019). "Autonomous Deployment of a Solar Panel Using Elastic Origami and Distributed Shape-Memory-Polymer Actuators". *Physical Review Applied* 11 (6), 064069. DOI: 10.1103/PhysRevApplied.11.064069.

Elghazi, Y., A. Wagdy, S. Mohamed, and A. Hassan (2014). "Daylighting Driven Design: Optimizing Kaleidocycle Facade for Hot Arid Climate". *Fifth German-Austrian IBPSA Conference RWTH Aachen University*, 314–321.

Espressif Systems (2025). *ESP32 Series Datasheet - Version 5.2.* Accessed February 2026. URL: https://documentation.espressif.com/esp32_datasheet_en.pdf.

European Committee for Standardisation (2005). *EN 1991-1-4: Eurocode 1: Actions on structures, Parts 1-4: General actions. Wind actions.* Authority: The European Union Per Regulation 305/2011, Directive 98/34/2011, Directive 98/34/EC, Directive 2004/ 18/EC.

Fonseca, L. M., G. V. Rodrigues, and M. A. Savi (2022). "An overview of the mechanical description of origami-inspired systems and structures".

International Journal of Mechanical Sciences 223, 107316. DOI: 10.1016/j.ijmecsci.2022.107316.

Fraternali, F., E. De Chiara, and R. E. Skelton (2015a). "On the use of tensegrity structures for kinetic solar facades of smart buildings". *Smart Materials and Structures* 24 (10), 105032. DOI: 10.1088/0964-1726/24/10/105032.

Fraternali, F., E. Babilio, R. Nazifi Charandabi, G. Germano, and G. Luciano Raimondo Spagnuolo (2024a). "Dynamic origami solar eyes with tensegrity architecture for energy harvesting Mashrabiyas". *Applications in Engineering Science* 19, 100190. DOI: 10.1016/j.apples.2024.100190.

Fraternali, F., G. Carpentieri, and A. Amendola (2015b). "On the mechanical modeling of the extreme softening/stiffening response of axially loaded tensegrity prisms". *Journal of the Mechanics and Physics of Solids* 74, 136–157. DOI: 10.1016/j.jmps.2014.10.010.

Fraternali, F., J. de Castro Motta, G. Germano, E. Babilio, and A. Amendola (2024b). "Mechanical response of tensegrity-origami solar modules". *Applications in Engineering Science* 17, 100174. DOI: 10.1016/j.apples.2023.100174.

Gandolfo, A. (2023). *CNC SHIELD V3 per A4988/ DRV8825 Controller*. Accessed February 2026. URL: https://www.adrirobot.it/cnc-shield-v3-per-a4988-drv8825-controller/.

Gao, Y., J. Dong, O. Isabella, R. Santbergen, H. Tan, M. Zeman, and G. Zhang (2018). "A photovoltaic window with sun-tracking shading elements towards maximum power generation and non-glare daylighting". *Applied Energy* 228, 1454–1472. DOI: 10.1016/j.apenergy.2018.07.015.

Garcia-Sanchez, A., G. Vallerotto, S. Askins, I. Antón, and C. Domínguez (2025). "A smart semi-translucent building-integrated PV module based on integrated-tracking micro-concentration providing high power density and active daylight management". *Solar Energy Materials and Solar Cells* 287, 113246. DOI: 10.1016/j.solmat.2024.113246.

Goodman, R. S. and L. C. Meier (2013). *Wind-resistant retractable awning*. (U.S Patent 2013/0213587 A1).

Holmes, J. D. (2018). *Wind Loading of Structures*. 3rd ed. CRC Press. ISBN: 9781351229142. DOI: 10.1201/b18029.

Karanouh, A. and E. Kerber (2015). "Innovations in dynamic architecture". *Journal of Facade Design and Engineering* 3 (2), 60–73. DOI: 10.3233/fde-150040.

Li, Y. and S. Pellegrino (2020). "A Theory for the Design of Multi-Stable Morphing Structures". *Journal of the Mechanics and Physics of Solids* 136, 103772. DOI: 10.1016/j.jmps.2019.103772.

Liu, Z., H. Fang, J. Xu, and K. Wang (2023). "Digitized design and mechanical property reprogrammability of multistable origami metamaterials". *Journal of the Mechanics and Physics of Solids* 173, 105237. DOI: 10.1016/j.jmps.2023.105237.

Lu, L., J. Dai, S. Leanza, J. W. Hutchinson, and R. R. Zhao (2023a). "Multiple equilibrium states of a curved-sided hexagram: Part II—Transitions between states". *Journal of the Mechanics and Physics of Solids* 180, 105407. DOI: 10.1016/j.jmps.2023.105407.

Lu, L., S. Leanza, J. Dai, X. Sun, and R. R. Zhao (2023b). "Easy snap-folding of hexagonal ring origami by geometric modifications". *Journal of the Mechanics and Physics of Solids* 171, 105142. DOI: 10.1016/j.jmps.2022.105142.

Miranda, R., E. Babilio, N. Singh, F. Santos, and F. Fraternali (2020). "Mechanics of smart origami sunscreens with energy harvesting ability". *Mechanics Research Communications* 105 (103503). DOI: 10.1016/j.mechrescom.2020.103503.

Miura, K. (1985). "Method of packaging and deployment of large membranes in space". *The Institute of Space and Astronautical Science report* 618, 1–9.

Pesenti, M., G. Masera, F. Fiorito, and M. Sauchelli (2015). "Kinetic Solar Skin: A Responsive Folding Technique". *Energy Procedia* 70, 661–672. DOI: 10.1016/j.egypro.2015.02.174.

Pratapa, P. P., P. Suryanarayana, and G. H. Paulino (2018). "Bloch wave framework for structures with nonlocal interactions: Application to the design of origami acoustic metamaterials". *Journal of the Mechanics and Physics of Solids* 118, 115–132. DOI: 10.1016/j.jmps.2018.05.012.

Salazar, R., S. Murthy, C. Pellazar, and A. Stoica (2017). "TransFormers for lunar extreme environments: Large origami deployable solar reflectors". *2017 IEEE Aerospace Conference*, 1–7. DOI: 10.1109/AERO.2017.7943717.

Schenk, M. and S. D. Guest (2013). "Geometry of Miura-folded metamaterials". *Proceedings of the National Academy of Sciences of the United States of America* 110 (9), 3276–3281. DOI: 10.1073/pnas.1217998110.

Seffen, K. A. (2012). "Compliant shell mechanisms". *Philosophical Transactions of the Royal Society A: Mathematical, Physical and Engineering Sciences* 370.1965 (1965), 2010–2026. DOI: 10.1098/rsta.2011.0347.

Seffen, K. A. and S. R. M. Pellegrino (1997). *Deployment of a rigid panel by tape-springs*. Tech. rep. Department of Engineering, University of Cambridge, CUED/DSTRUCT/ TR168.

Shabana, A. A. (1996). "Continuous Systems". *Theory of Vibration: An Introduction*. Springer New York, 301–336. ISBN: 978-1-4612-3976-5. DOI: 10.1007/978-1-4612-3976-5_7.

Su, N., S. Peng, and N. Hong (2018). "Analyzing the background and resonant effects of wind-induced responses on large-span roofs". *Journal of Wind Engineering and Industrial Aerodynamics* 183, 114–126. DOI: 10.1016/j.jweia.2018.10.021.

Sumner, R. W. and J. Popović (2004). "Deformation transfer for triangle meshes". *ACM Transactions on Graphics* 23 (3), 399–405. DOI: 10.1145/1015706.1015736.

Vassiliades, C., R. Agathokleous, G. Barone, C. Forzano, G. F. Giuzio, A. Palombo, A. Buonomano, and S. Kalogirou (2022). "Building integration of active solar energy systems: A review of geometrical and architectural characteristics". *Renewable and Sustainable Energy Reviews* 164, 112482. DOI: 10.1016/j.rser.2022.112482.

Wagdy, A., Y. Elghazi, S. Abdalwahab, and A. Hassan (2015). "The balance between daylighting and thermal performance based on exploiting the kaleidocycle typology in hot arid climate of Aswan, Egypt". *AEI 2015: Birth and Life of the Integrated Building - Proceedings of the AEI Conference 2015*, 300–315. DOI: 10.1061/9780784479070.028.

Willmott, K. (2019). *SolarPosition - Arduino Library to calculate the position of the sun relative to geographic coordinates*. Accessed February 2026. URL: https://github.com/KenWillmott/SolarPosition/blob/master/SolarPosition.h.

Wittwer, A. R., J. M. Podestá, H. G. Castro, J. L. Mroginski, J. O. Marighetti, M. E. De Bortoli, R. R. Paz, and F. Mateo (2022). "Wind loading and its effects on photovoltaic modules: An experimental–Computational study to assess the stress on structures". *Solar Energy* 240, 315–328. DOI: 10.1016/j.solener.2022.04.061.

Zhai, Z., Y. Wang, and H. Jiang (2018). "Origami-inspired, on-demand deployable and collapsible mechanical metamaterials with tunable stiffness".

Proceedings of the National Academy of Sciences of the United States of America 115 (9), 2032–2037. DOI: 10.1073/pnas.1720171115.